The protocol for mesoscopic wide-field optical imaging in mice: from zero to hero

Kislukhina E.N.[1], Lizunova N.V.[1*], Surin A.M.[2], Bakaeva Z.V.[1,3#]

[1]Laboratory of Neurobiology and Fundamentals of Brain Development, National Medical Research Center for Children's Health Federal state autonomous institution of the Russian Federation Ministry of Health, Moscow, Russia

[2]Laboratory of fundamental and applied problems of pain, Institute of General Pathology and Pathophysiology, Moscow, Russia

[3]Department of Pharmacology, A.P. Nelyubin Institute of Pharmacy, I.M. Sechenov First Moscow State Medical University (Sechenov University), Moscow, Russia

Correspondence:
[*]Natalia V. Lizunova
natalia.lizunova18@mail.ru

[#]Zanda V. Bakaeva
zv.bakaeva@gmail.com

Keywords: cranial window, skull thinning, calcium imaging, hemodynamics, intrinsic brain signals.

Abstract

This article provides protocols that make possible to master mesoscopic wide-field optical brain imaging from scratch. The protocols describe surgery for wide-field cranial window creation in mice, and wide-field imaging process and setup. The protocols for components of imaging system selection and assembly, creation of a headplate for fixation, and mice training are also provided. The last part briefly describes methods for data processing.

The above procedure can be used to visualize dorsal cortex via wide-field optical imaging as well as laser-speckle contrast imaging methods. The distinguishing features of our protocol are: a wide cranial window (up to 60% of the entire cortex), scull thinning (without craniotomy), ultraviolet-curable transparent coating (gel polish), measurements in awake behaving mice. During the surgery the helicopter-like headplate with its lower surface congruent to scull surface is mounted on mouse head. This headplate is lightweight and enable to fix head securely during movement to avoid frames alignment during data processing. Cranial window remains sufficiently transparent for at least 3 months.

Wide-field optical imaging method enables to record brain haemodynamics and energy metabolism (FAD concentration dynamics) in wild-type mice. Use of transgenic animals expressing genetically-encoded sensors enable measurements of ions concentration (e.g. Ca^{2+}-dynamics) and other compounds (e.g. glutamate). The article describes measurements by wide-field optical imaging of oxy-, deoxy-, and total haemoglobin concentrations changes in combination with various intracellular parameters: Δ[FAD] or $\Delta[Ca^{2+}]$ or ΔpH with $\Delta[Cl^-]$.

Introduction

In vivo imaging techniques are rapidly advancing in biological research, offering significant advantages over traditional histological and biochemical methods. These techniques allow for

chronic studies within the same animal, reducing the number of subjects required and enhancing data quality. Notably, *in vivo* brain imaging can now be performed in awake animals, eliminating anesthesia-related confounds (Khiroug & Verkhratsky, 2021).

Among the neuroimaging techniques can be highlighted traditional, used in both experiment and clinic: structural and functional MRI, computer tomography, electroencephalography, electrocorticography, implanted electrodes, ultrasonic (doppler) imaging. However, optical methods have gained prominence in experimental neuroscience, including two- and three-photon microscopy, miniscopy, Raman microspectroscopy, laser speckle contrast imaging (LSCI), and wide-field optical imaging (WFOI) (Fedotova et al., 2023; Markicevic et al., 2021). A recent achievement is application of optical techniques (functional near-infrared spectroscopy – fNIRS) to humans (Li et al., 2022). WFOI, employing a cortex-wide cranial window, enables high spatial and temporal resolution imaging but is limited by light scattering, restricting depth measurements to the cerebral cortex (Padawer-Curry et al., 2023).

Brain activity can be observed due to the optical properties of haemoglobin, FAD and artificially created biosensors. The excitation of neurons causes vasodilation and an increase in local blood flow by the mechanism of neurovascular coupling. This is accompanied by an increase in total (HbT) and oxygenated haemoglobin (HbO) and a decrease in deoxyhaemoglobin (HHb). In addition, electrical activity requires the consumption of energy substrates (e.g. reduced flavine adenine dinucleotide), which is followed by an increase in the ratio [FAD]/[FAD-H_2]. Changes in FAD and haemoglobin concentrations can be measured photometrically, since haemoglobin is a pigment and absorbs light in the visible part of the spectrum (the absorption spectrum is different for HbO and HHb), and FAD (but not FAD-H_2) has fluorescent properties (Chance et al., 1979; Kozberg et al., 2016). The use of genetically encoded fluorescent sensors allows to expand the panel of visualized processes. Among all genetically encoded sensors, the most widely used is the Ca^{2+}-sensor GCaMP (Dana et al., 2014; Y. Zhang et al., 2023), however, there are also sensors for pH, Cl^-, glutamate, etc (Arosio et al., 2010; Day-Cooney et al., 2023; Diuba et al., 2020a, 2020b; Kotova et al., 2023; Marvin et al., 2018). An increase in the concentration of a particular ion or molecule causes an increase in fluorescence or quenching of a sensor. For such experiments, transgenic mouse lines are used or viral transduction is carried out to express protein sensors in brain cells. All optical neuroimaging methods require the creation of a cranial window enabling optical access to the brain, which is achieved in various ways.

One advantage of wide-field optical neuroimaging is its ability to capture signals from a large area of a dorsal part of a cerebral cortex (dorsal cortex) simultaneously (Fig. 1). While signal detection through an intact skull is possible, it is affected by diploic vessel activity and significant light scattering. To overcome these issues, researchers either perform a craniotomy or thin the skull. The latter is a less invasive approach but requires specific skills to achieve optimal results.

Another key advantage is the ability to record brain activity in awake animals. This requires the development of a system that ensures stable head fixation while allowing for the simulation of free movement.

Additionally, wide-field optical neuroimaging offers remarkable versatility. By integrating different LEDs (light-emitting diodes), stimulus delivery devices, genetically encoded sensors, researchers can address a wide range of experimental questions. While commercial imaging systems are available, many laboratories prefer to assemble custom setups using various components to better suit their specific research needs.

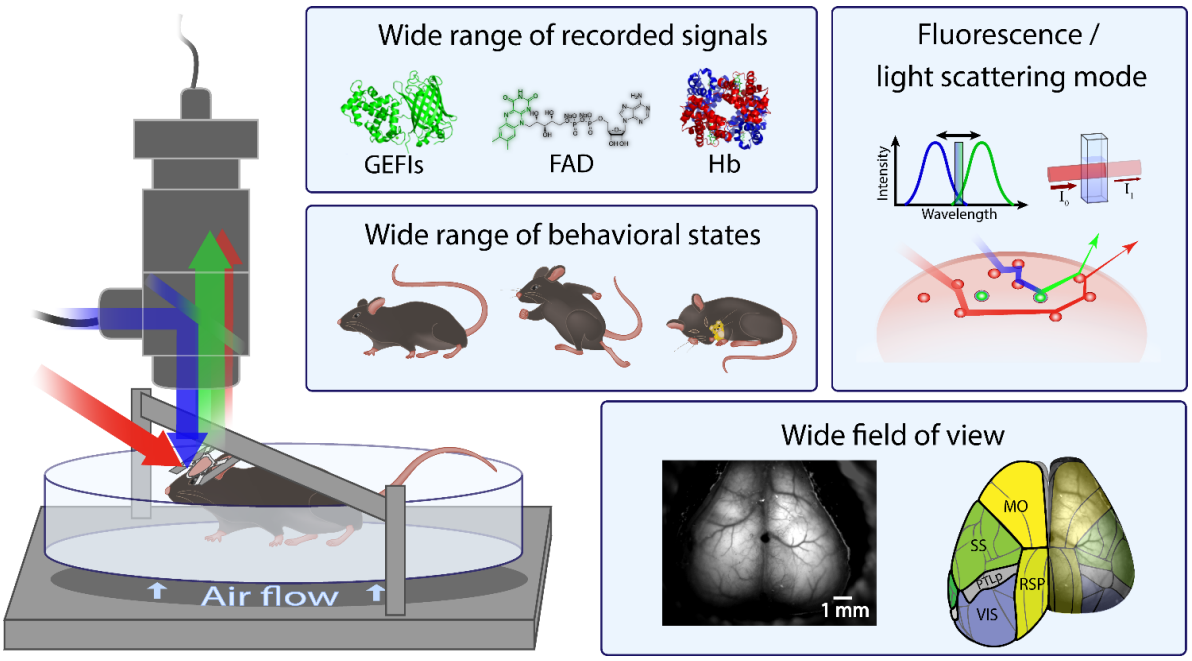

Figure 1. The main advantages of wide-field optical imaging. Wide-field optical imaging enables measurement of changes in the concentrations of endogenous fluorophores (e.g., FAD) and pigments (e.g., haemoglobin, Hb), as well as signals from artificial genetically encoded fluorescent indicators (GEFIs), in both awake freely moving animals and anesthetized ones. Measurements can be performed in fluorescence or light scattering (reflectance, intrinsic optical signal) modes. A wide cranial window allows visualization of all major cortical regions, except the auditory cortex. MO – Somatomotor areas; PTLp – Posterior parietal association areas; RSP – retrosplenial area; SS – Somatsensory areas; VIS – visual areas according to the Allen mouse brain common coordinate framework (Q. Wang et al., 2020).

Our protocols provide a step-by-step guide to cranial window preparation by skull thinning with a transparent protective coating, imaging system assembly, and animal training for imaging sessions. By outlining an effective and adaptable approach to WFOI, we aim to make high-precision neural imaging more accessible to researchers. The protocols were extensively tested and refined. Selected results have been published in (Kislukhina et al., 2023).

Materials and Methods

The equipment, tools, and consumables used in this study are listed in Supplementary Table S1.

1. Headplate design

This section describes the process of manufacturing headplates (Fig. 2) that are compatible with the Mobile Homecage® system (Neurotar, Finland). This headplate design have the following advantages: wide field of view; lightness and compactness; congruence to the surface of the scull; secure head fixation during imaging, preventing frame alignment issues during data processing.

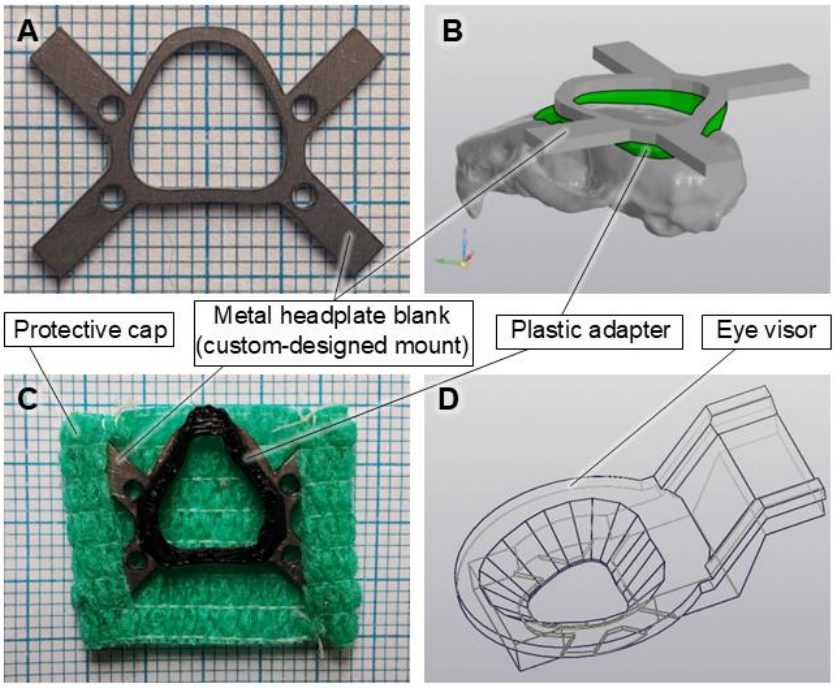

Figure 2. A headplate for securing an animal's head under a microscope. A) A titanium headplate blank (custom-designed mount); B) A 3D-model for adapter that is congruent with the surface of the mouse's skull; C) The whole headplate: metal blank with glued plastic adapter and a removable protective cap (ventral view); D) A 3D-model for visor, which prevents eye stimulation from LEDs of illumination system.

The protocol describes headplate manufacturing from two parts: a metal blank and a concave adapter made of plastic. At the end of the protocol, a method for manufacturing a brain surface protective cap that prevents injury is described. The Supplementary file S2 provide alternative protocols for headplate design.

1.1. Manufacturing headplates

1. Order laser-cut flat reusable headplate blanks from a 1 mm thick sheet of steel or titanium according to the drawing (see Supplementary file S3).

Note: Titanium is preferred because it is lighter and does not corrode.

2. Print the black PET-G plastic headplate adapters using a 3D printer (for 3D model please see Supplementary file S3). If needed, refine it with a needle file.

Note: The black color of the plastic prevents light from penetrating through the headplate.

3. Degrease surfaces. Apply cyanoacrylate glue to the metal workpiece. Place plastic headplate adapters on top to match contours of two items. Press firmly for 10 s and allow to dry for 1-2 minutes (Fig. 2).

Note: If these headplates do not meet your requirements, please see Supplementary file S2 for alternative protocols including custom adapters creation from epoxy resin.

4. 3D-print eye visor using the black PET-G plastic (for 3D model please see Supplementary file S3).

5. Cut 20x32 mm piece of veterinary bandage with bitter impregnation. Fold a 4-mm parts on each side to make 20x24 mm piece. Sew it up to make two pockets for

«propeller blades» of the helicopter-like headplate (Fig. 2C). Test if it is easy to put it on and off. The cap should not touch mouse's eyes.

Note: The protective cap prevents brain damage and dust ingress. The cap is essential for keeping male mice together, as they prone to fighting. It is not strictly necessary for solitary confinement or for keeping females together.

1.2. Reuse of metal blanks

6. Remove the headplate from the mouse's head at the end of an experiment. Place the headplates in acetonitrile for a minimum of 2 hours to dissolve dental resin and glue.

7. Remove any remaining glue and plastic with sandpaper or a needle file.

2. Wide-field thinned cranium surgery

This section describes a surgical procedure to create a wide cranial window (Fig. 3). The main advantages of this protocol over craniotomy include: lower invasiveness, as the cranial cavity remains intact, low risk of bleeding, and ease of coating. The main limitations include bone regrowth if osteogenic layer was not removed completely, and requirement of delicate surgical technique as neuroinflammatory response may occur. For video-protocol see https://www.youtube.com/@WIFIOPIA. Detailed techniques and material specifications are available in Supplementary table S1 and Supplementary file S2. Troubleshooting guide is in Supplementary file S4.
All experiments with animals should be conducted in accordance with local ethical guidelines.

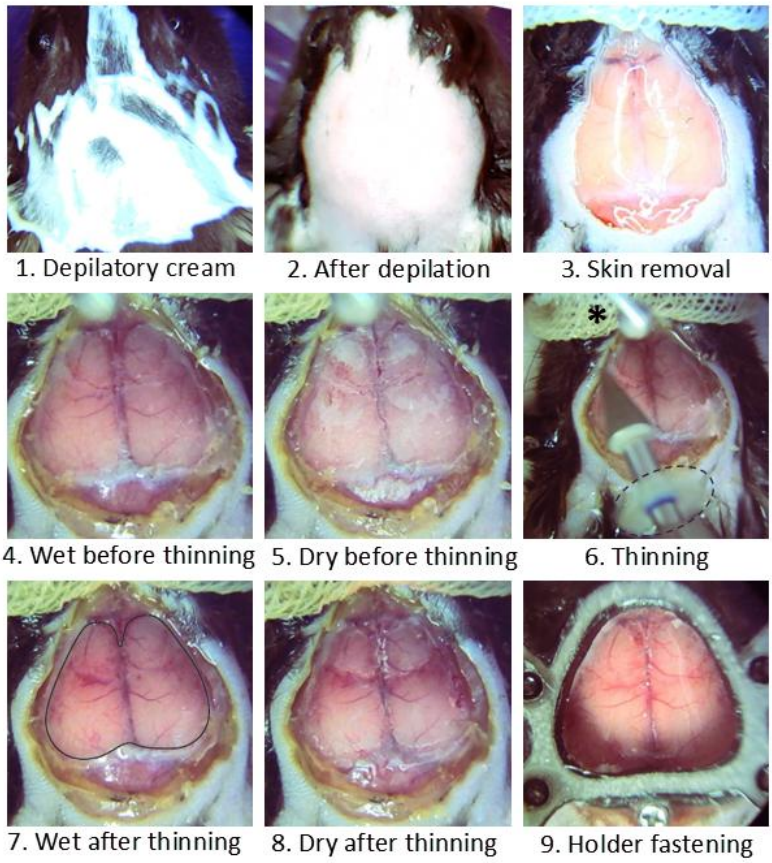

Figure 3. Stages of the surgery. 1. Apply depilatory cream for 1-5 min. 2. Remove depilatory cream with nail stick and damp cotton swab. 3. Sterilize surgical field; remove skin and fascia. 4. Set up continuous rinsing with saline using peristaltic pump; use gauze for drainage. 5. Check skull thickness periodically by drying with air flow. 6. Thin skull using microdrill with progressively softer milling cutters; * – tip of saline needle and drainage gauze, under the head cotton wool is placed for saline absorbance; ◌ – protective "skirt" for milling tool to prevent fluid from entering the drill. 7. Wet thinned skull have minimal differences from the intact one; ○ – thinned area. 8. Good visibility of blood vessels trough dry scull indicates proper thinning. 9. Secure the screw into the occipital bone; fasten holder with cyanoacrylate glue and dental resin; cover skull with cyanoacrylate glue, base and top gel polish.

2.1. Preparation for surgery. Perform one day or more before surgery

1. Cover all work surfaces and equipment with plastic film, leaving ear bar tips, dental clamp fronts, binocular lenses, light source, and tip of saline needle (see 2.1.7) uncovered.

2. Prepare protective "skirts" for milling tools by cutting ~7 mm plastic discs with central holes matching the cutter shaft. Secure ~5 mm from the tip using gel polish.

Note: Steps 1-2 prevent fluid from entering the drill and other equipment.

3. Prepare aseptically the following solutions (Table 1): Marbofloxacin (0.00017 mg/mL in water for injection), Ketoprofen (1.65 mg/mL in saline), and Dexamethasone (0.35 mg/mL in saline). Store at +4 °C in aliquots.

Table 1. Medications.

Reagent	**Final concentration**	**Amount**
Marbofloxacin 0.00017 mg/mL solution		
Marbobel 2 (Marbofloxacin 20 mg/mL)	91.7%	11 ml
Water for injection	8.3%	1 ml
Ketoprofen 1.65 mg/mL solution		
Ketonal (Ketoprofen 50 mg/mL)	3.3%	0.5 ml
Saline (0.9% NaCl)	96.7%	14.5 ml
Dexamethasone 0.35 mg/mL solution		
Dexamethasone for injection (Dexamethasone 4 mg/mL)	8.8%	132 µl
Saline (0.9% NaCl)	91.2%	1368 µl

4. Prepare angled cannula tips 18G, 45°; bend 27G needles to L-shape for skull cleaning, glue application, bubble removal, and to semi-C-shape for lacquer marking.

5. Make visor from aluminum foil to protect mouse's eyes from UV light.

6. Cut gauze into 2x6 cm strips and prepare cotton swabs and cotton wool for cleaning and drainage; store small supplies in one place for convenience.

7. Route silicone tubing from the peristaltic and air pumps to the above stereotaxic frame, attaching appropriate tips or needles for fluid delivery and airflow control.

Notes:
– Immediately dry and rinse equipment with distilled water if saline contact occurs to prevent corrosion.
– Marbofloxacin may precipitate in saline; use water for dilution.

2.2.Surgery

Preparation for surgery. Perform on the day of the operation

1. Check availability of all tools, materials, and medications.
2. Disinfect the workspace, instruments, and screws (avoid heating for headplates; they can be treated briefly with 70% ethanol prior to gluing).
3. Prepare materials for cleaning depilatory cream (distilled water, nail stick, swab) and a clean cage with food and water.
4. Flush perfusion pump tubing with 50 ml 6% peroxide, 50 ml distilled water, and 25 ml saline, unless reused consecutively.
5. Set up the perfusion pump by hanging a 200 mL saline infusion bag, and connect it to the pump tubing. Configure the flow rate to 1–2 mL/min.
6. Turn on the temperature-controlled pad (37 °C).

Animal preparation

7. Anesthetize the animal in the induction chamber of the isoflurane system (4% isoflurane).
8. After anesthesia induction, quickly shave the surgical area using an electric shaver.
9. Transfer the animal to the stereotaxic frame, and reduce isoflurane to 1–2.5% to maintain stable anesthesia.
10. Apply eye gel regularly (~every 15 min) to prevent drying.
11. Administer dexamethasone intramuscularly (0.7 mg/kg).
12. Insert and secure a lubricated rectal probe.
13. Inject 0.1 mL of 0.2% lidocaine subcutaneously under the scalp.
14. Place cotton wool under the head to absorb saline.
15. Adjust microscope and lighting for binocular viewing.

Preparation of the surgical field

16. Apply depilatory cream to the scalp for 1–5 minutes (depending on freshness), covering a slightly wider area than the planned incision; remove cream and fur using a nail stick, then clean the skin with a damp cotton pad (Fig. 3, the panels 1-2).

17. Disinfect gloves and clean the mouse's head three times with 70% ethanol and povidone-iodine antiseptic.

Note: Avoid ethanol and depilatory cream to contact eyes.

18. Confirm absence of pedal reflex.

19. Excise the scalp to expose the occipital, parietal, frontal, and part of the nasal bones; do not expose muscles; ensure smooth incision edges (Fig. 3, the panel 3).

20. Control capillary bleeding by applying topical haemostatic agent for 1-2 min.

21. Remove all connective tissue from the skull surface, including edges, to ensure proper headplate fixation and prevent interference with drilling.

Thinning of the skull

23. Place saline-soaked gauze over the nasal bones, covering the eyes and retracting the vibrissae.

24. Ensure stable head fixation in the stereotaxic frame; reinforce ear bar placement if needed.

25. Activate the peristaltic pump (1–2 mL/min) and adjust the saline needle to ensure that saline drop lands rostral to the thinning site.

26. Set the microdrill speed (~25,000 rpm) and insert the diamond medium-grit diamond bur.

27. Place index and middle fingers of non-dominant hand on ear bars. Stabilize your working hand by resting little finger and ulnar side on top of the index finger or heating pad, then begin skull thinning with the microdrill.

28. First, thin the frontal bones; control bleeding as needed (Fig. 3, the panel 6). Maintain tangential motion for uniform thinning.

29. Slightly thin the sutures, avoiding over-thinning near the rostral ¼ of superior sagittal sinus (Fig. 3, the panel 7).

30. Stop the drill and pump; dry the skull with airflow and assess thinning. Pinkish areas indicate adequate thinning (Fig. 3, the panels 4-8).

31. Resume thinning of the parietal bones with continuous movements across the sagittal suture.

32. Refine thinning of the sutures. Pay special attention to frontal bones boundaries as they prone to regrowth. Polish the surface using progressively softer cutters: medium-grit silicone-diamond polisher (blue), fine-grit (red), then extra-fine grit (grey). Leave the inner bone layer intact.

33. Continue until the skull is uniformly transparent when both wet and dry, with visible vasculature.

Notes:
– Stable head fixation and drilling hand stabilization reduce risk of brain injury.
– Proper drainage prevents mouse aspiration and keeps optics clean.

– Bleeding may occur from diploic vessels, this is expected.
– Uneven thinning increases fracture risk; avoid pressure near thinned (pinkish) areas.
– Avoid drying the fully thinned skull for extended periods.

Application of Coating and Headplate Fixation

34. Reapply eye gel and dry the skull (Fig. 3, the panel 8).
35. Apply a thin layer of cyanoacrylate glue to the thinned area using L-shaped 27G needle. Allow it to harden.
36. Confirm head stability and insert a M1 screw into a pre-drilled by tungsten carbide drill bit indentation in the occipital bone without penetrating fully.
37. Use scalpel blade №15 to score nasal bones for proper headplate fixation.
38. Sterilise and test-fit the headplate, then glue it in place with gentle pressure.
39. Shield the eyes with foil visor. Apply a layer of base coat of gel polish to the thinned skull. Cure under UV light for 15s, then for 60s. Repeat with a top coat.
40. Mark bregma with black nail polish if no longer visible. Use semi-C-shaped needle.
41. Prepare self-curing acrylic dental resin: mix ~0.2 g powder and 0.25 ml liquid in 5 mL silicone mixing cup. Apply it gradually around the headplate through syringe with angled cannula tips 18G, sealing the entire perimeter including skin edges, but avoiding contact with the cranial window or eyes (Fig. 3, the panel 9).
42. After the resin sets, remove the animal from the frame. Administer Marbofloxacin (8 mg/kg), Ketoprofen (8.5 mg/kg), and 0.5 mL saline subcutaneously.
43. Discontinue isoflurane and place the mouse in a clean, heated single-housing cage. Monitor for at least 1 hour after operation.
44. For the next 3 days, administer Marbofloxacin and Ketoprofen daily while monitoring recovery and inflammation.
45. Continue rehabilitation for at least 14 days (preferably 1 month) before experiments.

Notes:
– Cyanoacrylate glue eliminates the osteoblast population.
– Prevent bubble formation and blood ingress in glue, gel polish and resin.
– If possible, make flat surface with gel polish, glare may occur on the spherical surface.
– UV curing generates heat; use intermittent exposure to avoid thermal injury.
– Avoid excessive resin on the sides of the headplate to ensure proper holder mounting afterwards.
– Post-operative injections (antibiotic and analgetic) should be administered subcutaneously in the back area rather than into the scuff to avoid disturbing the surgical site.

3. Component selection and assembly for wide-field optical imaging system

This section describes the assembly and configuration of the WFOI system. The first part provides the minimal required configuration for measurement of changes in HHb or HbT only in anesthetized animal. The second part describes further modifications to enable measurement of multiple parameters — HbO, HHb, and HbT alongside FAD (in wild-type mice), or Ca^{2+} (in mice expressing GCaMP), or pH and Cl^{-} (in mice expressing ClopHensor) — as well as sensory stimulation in awake, behaving animals.

The system can be easily modified for laser speckle contrast imaging or adapted for different fluorescent sensors. The limitation is the short-wavelength range (up to 430 nm), as it penetrates poorly through the skull coating.

The fundamental design of the imaging system is shown in Fig. 4. Since individual components used to build imaging systems may vary across laboratories, we have focused on general principles of component selection and assembly, rather than the specific details of our setup.

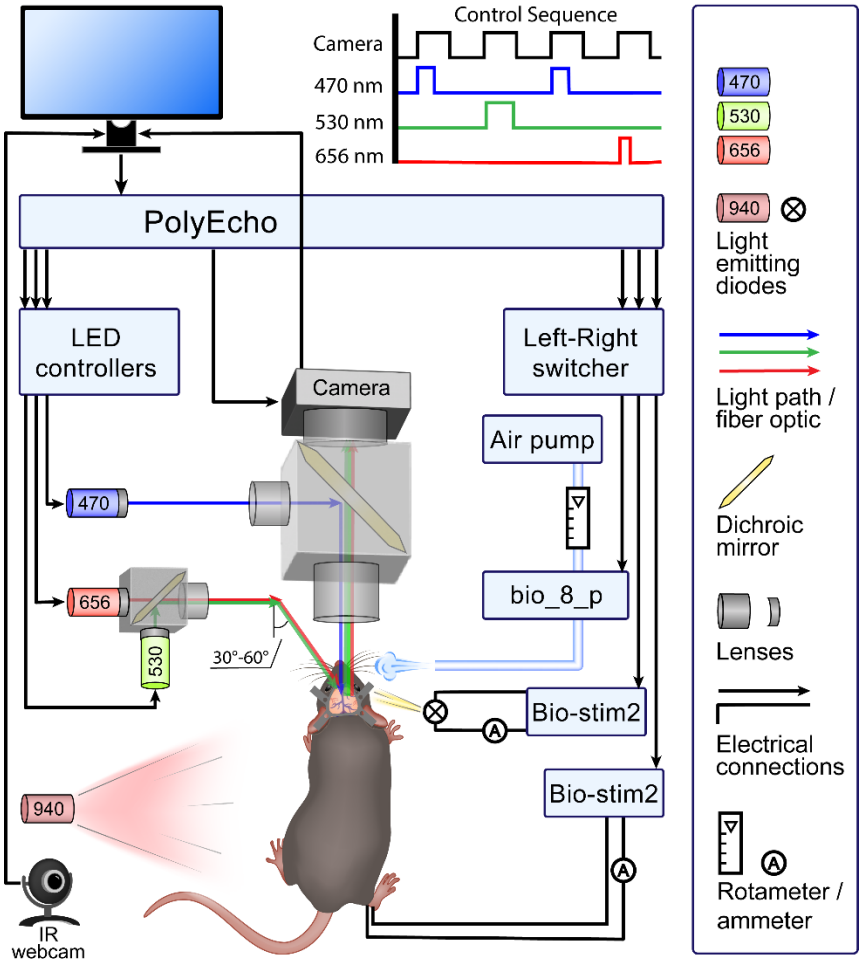

Figure 4. Schematic diagram of our WFOI system, with the illumination setup on the left and sensory stimulation devices on the right. IR webcam with LED 940 nm records mouse behavior.

3.1. The minimum configuration

The minimum configuration for a WFOI system includes:

- one LED for haemoglobin imaging;
- LED controller to regulate current;
- lens;
- camera for image acquisition;
- LED stand;
- camera stand;
- two tables;
- computer;
- software for controlling the camera and the LED controller;
- multi-channel controller to synchronize the LED controller, the camera, and the computer;
- head-fixation frame;

- heating pad for the mouse.

This setup is enough for measuring Δ[HbT] or Δ[HHb] (depending on the chosen LED wavelength; see Table 2) in an anesthetized animal.

Optional components that can enhance the system include: uninterruptible power supply (UPS), an actively vibration-isolated table, a bandpass filter, collimating and focusing lenses, a light diffuser, an external hard drive.

In our setup, the core system consists of an collimated LED 530 nm for HbT (BLS-LCS-0530-03-22, Mightex, CA, USA); a 530 nm bandpass filter (ZET532/10x, Chroma Technology Corp., VT, USA); a BioLED light source control module (BLS-1000-2, Mightex, CA, USA); lenses (OBJ-MAO-020-LWD, MAO-1-25-G-1C, Mightex, CA, USA); a high-sensitivity camera (CXE-B013-U, Mightex, CA, USA); a rectangular U-shaped LED mounting stand (Thorlabs, NJ, USA); an XYZ-motorized camera system (Zaber, Canada; Mightex, CA, USA), an U-shaped stand for motorized system (Thorlabs, NJ, USA; Micro Control Instruments Ltd., England); a custom-made anti-vibration table 75x270 cm and a secondary table for a mouse with a keyboard; a Back-UPS (ES 700VA, APS, USA); PolyScan4 and BuffCCD Cam software (Mightex, CA, USA); Legion T5 26IOB6 computer (Lenovo Group Limited, China), and a GeForce 3060 Ti GPU (NVIDIA, USA); a WDBWLG0040HBK-XB 6 TB (Western Digital, Thailand); a 12-channel PolyEcho Intelligent I/O Control Module BLS-IO12-U (Mightex, CA, USA); a Mobile HomeCage® (Neurotar, Finland), and a ThermoStar Homeothermic Monitoring System (RWD, China). The detailed description of mounting stands and computer characteristics is provided in Supplementary table S1.

Note: Based on our experience, the camera, the BuffCCD Cam software, the anti-vibration table, and the UPS included in the system are not optimal and may benefit from replacement. The equipment does not necessarily have to be expensive (see Discussion section), but a high-sensitivity camera is crucial for achieving a good signal-to-noise ratio.

3.1.1. Room, electrical supply and stands

1. Choose a dedicated recording room. Light, noise and vibrations can interfere with imaging, therefore, cover windows with roller shutters.

Note: Temperature control in the room is important to prevent LED overheating.

2. Set up a table for the LED, the camera and a head-fixation frame. An actively vibration-isolated table is recommended. Set up one more table for the devices, which can cause vibrations (such as computer).

Note: Ensure that the monitor light does not reach the experimental setup. Arrange the monitor behind the mouse to prevent unintended visual stimulation.

3. All critical equipment should be backed up with an UPS of proper VA capacity (online UPS is optimal). Connect the UPS (or multiple units if required) to power outlets connected to separate electrical circuits.

4. Install the head fixation stand, e.g. a stereotaxic frame. Assemble the LED mounting stand and the camera stand.

Note: At least one of the camera stand or the head frame should be movable to enable focusing. Secure all screws tightly to prevent vibrations. To further prevent vibrations, you may screw up stands to tabletop. If frame displacement exceeds a pixel, post-recording alignment will be necessary (see 5.1).

3.1.2. Optical system

1. Assemble the LED for light scattering to its stand to provide lighting at an angle 30–60°. We recommend LED models with passive cooling and central wavelength 530 or 590 nm for HbT and 625 nm for HHb. The use of one LED will not allow precise measurements as HbO and HHb spectra overlap (Fig. 5). To measure the Δ[HbT] and Δ[HHb] presicely see 3.3.3.1 and 5.2.2.

Note: A 90° angle lighting for scattering would create glare from the skull surface, interfering with brain activity observations.

2. Add a bandpass filter of ~20 nm bandwidth after the LED to improve measurement accuracy. The recommended LED output power is 200–500 mW, if a narrow bandpass filter is used.

Note: Lower-power LEDs or optical filters with a narrower bandwidth may require longer exposure times (10–20 ms) — ensure this is acceptable for your experiment.

3. Mount collimating lenses to direct LED light. This reduces light loss.

Note: LEDs may serve as an unintended visual stimulus for the mouse.

4. Connect the LED to the LED controller. The controllers must automatically trigger the LED and manage the electrical current (not voltage) supplied to the LED to regulate brightness. Consider the maximum allowable current for the LED.

Note: Use LEDs and LED controllers from the same manufacturer.

5. Set up a light diffuser between the LED and a mouse. You can make it from glass or PET plastic sanded with sandpaper. Another option is to use a circular polarizing filter mounted on the lens, but it reduces the overall image brightness by 75% or more.

Note: A diffuser helps to eliminate glare. Surface irregularities of the skull become more noticeable, but this do not hinder the recorded brain activity.

6. Select a camera. We recommend using a monochrome camera with external trigger control (TTL signal), a frame rate of 100 Hz at a resolution of at least 256×256 pixels, and low dark current. However, a maximum frame rate of 10 Hz is sufficient for HHb- or HbT-only measurement (if the camera dark signal is not zero, increase the frame rate to capture dark frames; if the camera sensitivity is low, increase the frame rate for subsequent temporal binning). The captured images should have a bit depth of at least 16 bits.

Note: 8-bit images can also be used, but the processing quality will be lower. Resolution is not as critical; for WFOI analysis binning down to 64x64 pixels can be used. A camera with all pixels exposed simultaneously is preferable.

7. Attach the camera to the lens and set it up on the camera stand above the animal's head. A 2x – 4x lens with a working distance of 10 cm recommended.

Notes:

- *A lens with a shorter working distance will capture more signal but will make mouse manipulation more difficult.*
- *Although optional, steps 2-3, and 5 markedly enhance imaging quality.*

3.1.3. Control system

1. Connect the LED controllers to analog output of a multi-channel controller. Connect the camera TTL-trigger to a digital output. The multi-channel controller will transmit signals from a computer. The number of required channels depends on the number of wavelengths used—one per wavelength, one for the camera, and one per external device (e.g., a stimulator).

2. Connect all devices to a computer or a notebook. The appropriate computer should meet the following minimum system requirements: 16 GB of RAM, 512 GB of storage (preferably SSD), an Intel Core i5 or equivalent processor, and Windows 10/11 (64-bit), USB 3.0 support (at least four ports).

Note: For optimal performance, a computer with 64 GB of RAM, an Intel Core i7 (or equivalent) processor, and a dedicated graphics card (GPU) is recommended. Pay attention to the number of USB ports: at a full setup (see the following sections) eight ports will be occupied.

3. Install all necessary software for controlling the LEDs and the camera. This can be commercial software provided with the multi-channel controller and the camera or a third-party software (e.g. Micro-Manager 1.4 for camera (D. Edelstein et al., 2014)). The software should be capable of starting and stopping recordings, controlling the activation, intensity, and duration of LED illumination, adjusting camera exposure time, synchronizing frame exposure with LED activation, and configuring image-saving parameters (binning, gain, file format, automatic file names, save path). Additionally, it should allow pre-recording adjustments, including a preview mode for camera focusing and LED duration selection.

4. For raw data storage, select an external hard drive (6–8 TB).

3.2. LED illumination modules and lightguides

The LEDs combination in LED illumination modules is advisable for multi-wavelength illumination (see below). Liquid lightguides eliminate need for LED placement in close proximity of mouse's head, they also improve illumination angle and radius. LED grouping will simplify data processing later due to a uniform illumination pattern.

In our system we combined LEDs 530 nm and 656 nm with 1-7 fiber optic bundle in one module, and LEDs 460, 505, and 560 nm with single-fiber light guide in another module. Particular components depend on LED wavelength, please see 3.1, 3.2, 3.4, 3.5 for details.

1. Select appropriate beam splitters to combine LEDs for haemodynamic measurements into one assembly and those for fluorescence into another. Arrange the LEDs in the assembly in order of increasing wavelength (the shortest wavelengths closer to the optical fiber output). Ensure that each LED achieves >95% transmission or reflection.

Note: Alternatively, use one LED assembly both for Hb and fluorescence (for bright sensors).

2. Assemble the LED illumination modules: attach collimating lenses (see 3.1.2.3) to the LEDs, place bandpass filters (see 3.1.2.2 and 3.4.2) into the designated recesses on the beamsplitter, and affix each LED to the beamsplitter. Connect a lightguide adapter with focusing lens to the beamsplitter's output.

Note: Follow the manufacturer's recommended light direction for the dichroic mirrors. If LED power is suboptimal, use neutral density (ND) filters along with bandpass filters.

3. Connect a light guide to a lightguide adapter. The selected light guide must be long enough to allow camera movement. For fluorescence we recommend a 1-meter-long, 3-mm core diameter liquid light guide. For haemodynamics we recommend 1.2 m-long branched light guide (1–7) with 0.6 mm core diameter.

Note: Handle the light guide carefully to avoid end scratches and do not exceed the minimum bend radius. With high-power LEDs, it can be replaced by inexpensive optical fiber.

4. Adjust the light guide in a proper angle to the plane of the headplate: 30-60° for haemodynamics, 90° for fluorescence (see 3.1.2.1, 3.2.1 Note, and 3.4.2). It is optimal to adjust fiber optic bundle for haemodynamics around lens (see 3D model for mount in Supplementary file S3) to prevent shadows formation.

3.3. HbO, HHb and HbT measurements

HbO and HHb have different absorption spectra (Fig. 5). Two LEDs of wavelength with distinct molar extinction coefficients are enough to calculate both Δ[HbO] and Δ[HHb] (Ma et al., 2016).

Our HbO/HHb measuring system includes core system (see 3.1) and the following components: LED at 656 nm (LCS-0656-07-22, Mightex, CA, USA), bandpass filter (AT655/30m, Chroma Technology Corp., VT, USA), beam splitter (LCS-BC25-0605, Mightex, CA, USA), collimating lens with lightguide adapter (LGC-019-022-05-V, Mightex, CA, USA) 1-to-7 fan-out fiber optic bundle (BF76HS01, Thorlabs, NJ, USA) and custom-made mount for fiber optic bundle (see Supplementary file S3).

1. Select the second LED for haemodynamic imaging based on haemoglobin absorption spectra (Fig. 5). For intrinsic signal imaging only, we recommend 590 nm and 630 nm. If simultaneous GFP-based protein imaging used, we recommend 530 nm and 630 nm (Table 2, see also 3.1.2.1).

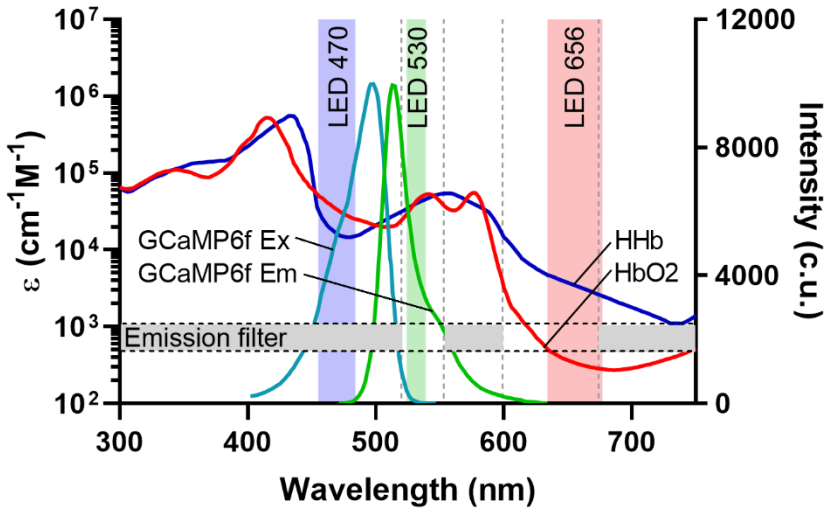

Figure 5. Optical spectra of our WFOI setup for measurement of oxyhaemoglobin (HbO) and deoxyhaemoglobin (HHb) alongside $\Delta[Ca^{2+}]_i$. Figure shows molar extinction coefficients for HbO and HHb, excitation and emission spectra of GCaMP6f. LED spectra shown after bandpass filers. The white sectors on the "Emission filter" stripe correspond to the emission filters transparency windows. The same configuration can be used for Δ[FAD] measurements in wild-type mice (not shown).

2. If available, assemble the LED illumination module with fiber optic bundle and mount for shadow-free illumination (see 3.2).

3. Connect the second LED to LED controller. If you have a 2-channel controller with a proper maximum current, use it for both LEDs.

4. Consider the frame rate (see 3.1.2.6), number of channels in the multi-channel controller (see 3.1.3.1) and the software requirements (see 3.1.3.3).

3.4. FAD and Ca^{2+} measurements

Due to strong overlap between excitation and emission spectra of FAD and GCaMP, fluorescent measurements of both Δ[FAD] and $\Delta[Ca^{2+}]_i$ can be performed using the same optical setup. Δ[FAD] can be measured in wild-type mice (e.g. C57BL/6J, IGB RAS, Russia), whereas $\Delta[Ca^{2+}]_i$ can be measured in transgenic animals, e.g. strain GP5.17 (JAX, stock #025393). FAD fluorescence is weak and FAD concentration changes are of low amplitude and therefore make minor (4-11%) contribution in Ca^{2+} measurements with GCaMP (Kozberg et al., 2016).

Fluorescent measurements require simultaneous measurements of Δ[Hb] as dynamically changing Hb absorbs both excitation and emission light (Ma et al., 2016; Valley et al., 2020).

In our setup fluorescent measurements of FAD and GCaMP are performed via LED 470 nm (BLS-LCS-0470-14-22-J, Mightex, CA, USA), bandpass filter (ET470/24m, Chroma Technology Corp., VT, USA), BioLED Light Source control module (BLS-3000-2, Mightex, CA, USA), liquid light guide (#77566 3-mm diameter, 1-m length, Thorlabs, NJ, USA), collimating lenses (LGC-019-022-05-V – 2 pc, EPI-MAO-LG, Mightex, CA, USA), and fluorescent cube (CUBE-MAO-CARR, Mightex, CA, USA) with filters (59009bs, 59026m, Chroma Technology Corp., VT, USA).

1. Select LED of excitation wavelength (470 nm for GCaMP, 460 or 470 nm for FAD). Use (*FPbase*, n.d.) to determine the optimal wavelength (Table 2). Required LED power depends strongly on fluorophore brightness, optical filters bandwidth, camera sensitivity, exposure and possibilities for temporal binning. In our setup 860 mW output power fits for both FAD and GCaMP measurements using spatial binning.

Table 2. Decision-make for LED wavelength choice. The preferred wavelengths are highlighted with underscore.

Measured molecules	LED's central wavelength	Reason
HbT	505 or <u>530</u> or 540 or 560 or <u>590</u>	Isosbestic points for HbO and HHb in green-red spectrum are 500, 530, 545, 570, and 584 nm. Use a narrow bandpass filter
HHb	<u>625</u>-680	HHb has a 10× higher molar extinction coefficient than HbO in the red spectrum. Between 625 nm and 680 nm HHb's extinction decreases significantly
HbT, HbO, HHb	590 and 625 nm	Longer wavelengths penetrate deeper into tissue, so yellow and red LEDs will sample similar depths (Ma et al., 2016). Theoretically, any two wavelengths are suitable. For optimal accuracy, one should be isosbestic and the other in the red region
HbT, HbO, HHb, GCaMP	530 and 625 nm for Hb 470 nm for GCaMP	530 nm is near emission maximum of GCaMP. Hb imaging is necessary for correction of fluorescence signals.

		430 nm may be used as Ca-independent signal of GCaMP (not necessary)
HbT, HbO, HHb, FAD	530 and 625 nm for Hb 470 nm for FAD	See above
HbT, GCaMP or FAD	530 for HbT 470 nm for GCaMP / FAD	One wavelength near emission maximum is enough for correction by regression method (Valley et al., 2020)
HbT, HbO, HHb, ClopHensor	530 and 625 nm for Hb 460, 505 and 560 nm for ClopHensor	See above
HbT, HbO, HHb, when intravenous dye is used (e.g., Rose Bengal)	E.g. 590 and 625 nm if Rose Bengal	Wavelengths outside dye absorption spectra

2. Assemble a fluorescence filter cube. Mount a bandpass optical filter facing toward LED, a dichroic mirror at a 45° angle and an emission filter facing toward the camera. They must prevent excitation light from entering the camera while efficiently transmitting light in the emission range. For examples, see (*Chroma Technology*, n.d.).

Note: The cube dimensions determine the filters diameter and therefore overall system cost.

3. Place a collimating lens between LED (or light guide if used, see 2.2) and the filter cube to transform the divergent light into a parallel beam.

Note: Inappropriate lens could create an interference pattern. Processing of such frames is complicated but possible.

4. Shield the LED light sources. Seal any gaps through which light could escape to prevent stray light from influencing recordings.

5. Consider the frame rate (see 3.1.2.6), number of channels in the multi-channel controller (see 3.1.3.1) and the software requirements (see 3.1.3.3).

3.5.Cl- and pH measurements

In transgenic mice expressing ClopHensor (Arosio et al., 2010; Diuba et al., 2020b; Ponomareva et al., 2021) ΔpH_i with $\Delta[Cl^-]_i$ can be measured via fluorescence. The setup includes LED illumination module with three LEDs for excitation (BLS-LCS-0455-03-22, BLS-LCS-0505-12-22, BLS-LCS-0560-03-22, Mightex, CA, USA), BioLED Light Source control module (BLS-1000-2, Mightex, CA, USA), bandpass filters (#65-142, Edmund Optics, USA; ET505/20x, ZET561/10x, Chroma Technology Corp., VT, USA), beam splitters (LCS-BC25-0480, LCS-BC25-0515, Mightex, CA, USA). The other parts remain unchanged as we select filters for fluorescence cube as universal for all three fluorophores (FAD, GCaMP6f and ClopHensor). LED 460 nm with narrow bandpass filter is crucial to reach an isosbestic point for pH and therefore measure $\Delta[Cl^-]_i$.

3.6. Recordings in awake animal

Anesthesia affects brain activity significantly, though both recording procedure and data processing in awake animal is complicated.

Our setup consists of the Mobile HomeCage® (Neurotar, Finland), a custom-made cage with transparent walls, a C-110 63110 webcam with a removed IR filter – 2 pc (Defender, China), and a Helios IR-Plate-2-940 illuminator – 2 pc (Microlight, China).

Note: Based on our experience, a C-110 63110 webcam is not optimal and may benefit from replacement.

1. Select an appropriate head fixation system, ensuring that it is safe for a mouse. The fixation system should be comfortable, adjustable in height, quick-to-secure and should not interfere with exploratory behavior.

2. Set up a movable platform under the head fixation system. This could be an air-supported cage, a treadmill, a rotating disk, or a spherical ball.

Note: An awake animal requires a system that permits running (preferably, in all directions) and grooming without head injury. An air-supported cage with opaque walls can create an illusion of free movement; however, we recommend transparent walls to enable behavioral video recording.

3. Mount the necessary components for behavioral video recording, including at least one infrared (IR) illuminator and one or more cameras.

Note: Behavior significantly affects brain activity, therefore it is essential to segment the recording into active and resting periods. Any spectrum outside the range captured by the brain imaging camera may be used; however, IR light is particularly suitable, as it is invisible to mice and does not introduce an additional sensory stimulus.

4. Set up additional components such as an airflow control unit and a pump.

3.7. Sensory stimulation

Sensory stimulation in awake animal simultaneously with WFOI is possible. Behavior interferes with stimulus response in brain, while anesthesia reduces brain activation dramatically. Sensory stimulation facilitates functional cortical mapping both under physiological conditions (e.g., throughout development) and in disease models (e.g., stroke), and allows for evaluation of the impact of external or experimental factors on fundamental brain functions.

Our stimulation system for eyes and hind limbs includes (Fig. 6): isolated constant current electrical stimulator (Bio-stim2, Biotechnologies, Russia); microammeter; white LED 3mm; custom-made left-right switcher; custom-made hind limb electrodes with tail clip.

Our stimulation system for vibrissae includes: air pump (607CD22, Thomas Industries Inc., USA); silicone air tubes of 10, 7, and 2 mm in diameter; rotameter (RWD, China); device for pinching of air tubes (bio_8_p, Biotechnologies, Russia).

White LEDs and air tubes are mounted on 3D-printed adapter for head fixation frame. We found optimal for LED light to be directed downward. Hind limb electrodes are clip-like, they are secured on tail clip with two soft springs. Electrodes are attached to ring-shaped piercing (2 rings per limb hooked on Achilles tendon) during recording. The piercing was fabricated from 27G needle, the electrodes were fabricated from segments of a second guitar string, and the tail clip from hair claw clip.

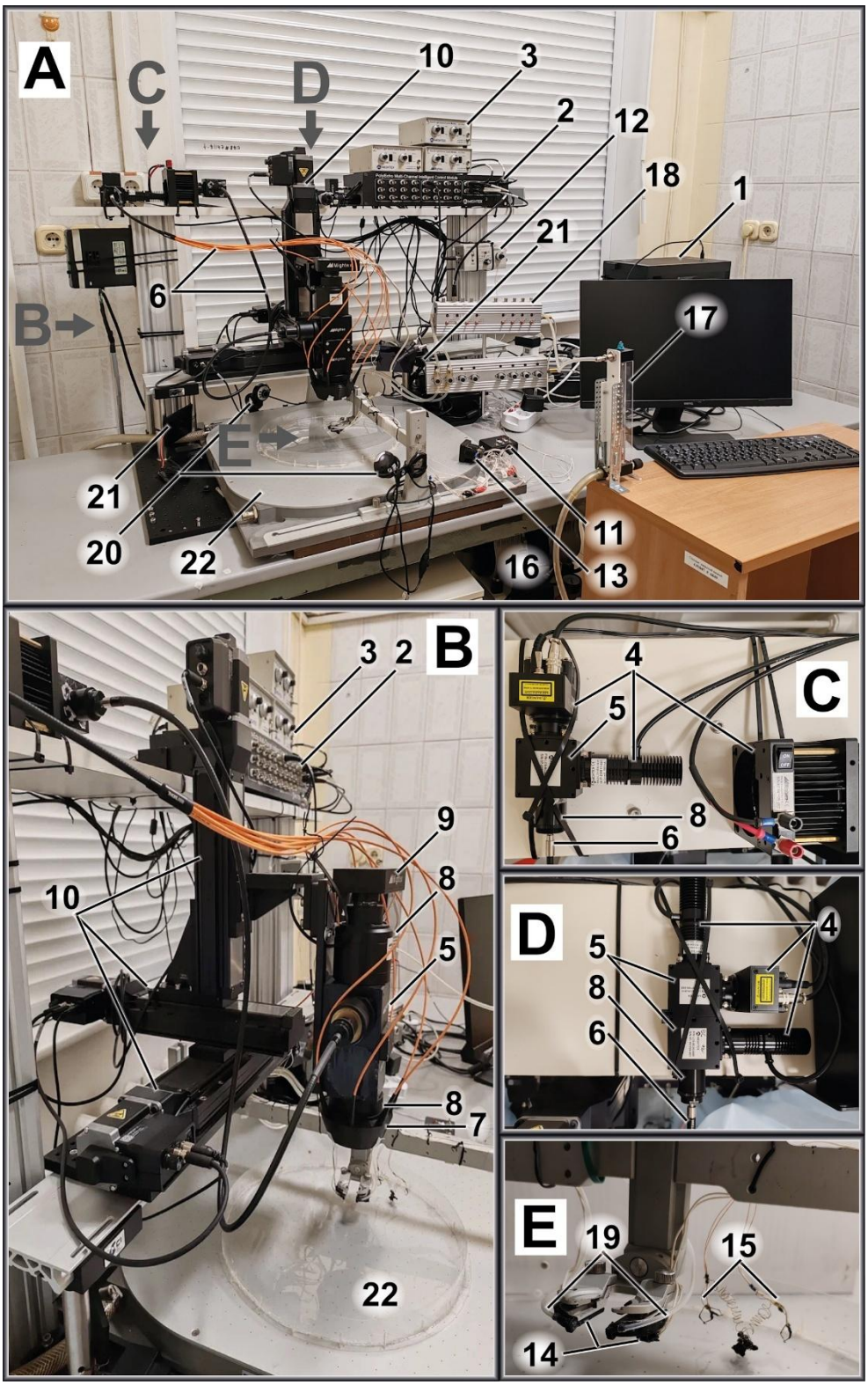

Figure 6. The whole WFOI setup.
Control system: 1 - Computer; 2 - PolyEcho; 3 - LED controllers;
Brain lighting and recording system: 4 - LEDs with bandpass filters; 5 - Cube with filters and dichroics; 6 - Fiber optic (1-1 and 1-7); 7 - 1-7 fiber optic mount; 8 – Lenses; 9 - CCD camera; 10 - Camera XYZ positioning;
Eye and limb stimulation: 11 - Left-right switcher; 12 - Electrical stimulator; 13 – Ammeter; 14 - White LED; 15 - Hind limb electrodes with tail clip;
Vibrissae stimulation: 16 - Air pump; 17 - Rotameter; 18 – bio_8_p (pinching of air tubes); 19 - Air tube;
Mouse fastening and behavior: 20 - Webcam with extracted IR-filter; 21 - IR LEDs; 22 - Mobile HomeCage (air pump is hindered).

4. Head fixation training and imaging process

This section describes animal habituation to head-fixation setup, parameter selection, and imaging procedure Since the configurations of setups and the objectives of experiments may vary across laboratories, we have aimed to describe general principles rather than focusing on the specifics of our setup.

4.1. Mouse habituation to head fixation

The habituation protocol acclimatises the mouse to head fixation in several stages. On day one, the mouse is familiarised with the room for 1h. Then mouse is gently restrained 3-5 times by the head in the handler's hands, then placed on a movable platform near head fixation apparatus for 1 min. On day two, the same steps are repeated, with addition of mouse restraining for short-time in the setup. On day three, the steps from day two are repeated, adding a longer head fixation (around one minute) in the apparatus, ending with lights off and LEDs on. Each manipulation is repeated at least three times, with rest periods in between. The aim is for the mouse to remain calm during fixation without associating the setup with negative experiences (for detailed SOP see Supplementary file S2, for troubleshooting guide see Supplementary file S4.).

Notes: Mice should be well-acclimated to handling before starting. Ensure the room's noise level matches experimental conditions.

4.2. Selection of imaging parameters

1. Select parameters according to your experimental goals. Choose a recording duration of 3–5 min for resting-state imaging or longer for stimulation protocols (at least 20 stimuli should be presented at 20-second intervals). Set the frame rate based on signal dynamics: ≥20 Hz for calcium imaging, 10 Hz for slower signals (Hb, FAD, Cl^-, pH). Define the LED sequence appropriate to the indicators used (e.g., LED470 → LED530 → LED470 → LED656 for GCaMP, HbT, HHb).
2. Configure the imaging system and triggering. Set up the software (e.g., PolyScan4) following manufacturer instructions, including LED models and controllers. Program an external TTL trigger matched to the frame rate with pulse duration < frame interval (e.g., 1 ms), and set the camera exposure time directly in the camera settings so that pulse duration does not affect it. The number of pulses = frame rate (Hz) × recording duration (s).
3. Set camera and exposure parameters. Use a fixed camera exposure time (e.g., 5 ms) for all recordings to avoid aliasing. Configure the camera to acquire 16- or 32-bit TIFF or RAW images at 256 × 256 resolution (with binning), gain = 0. Enable timestamp-based file naming and continuous preview mode.
4. Calibrate exposure and verify system performance. Place a 1 × 2 cm white paper with blue, green, and red markings in the field of view. Focus the camera, then gradually increase camera exposure for each LED until glare appears; set final LED exposure at 80 % of the glare threshold. If exposure values differ significantly, reduce the brightest LED's intensity (not below 50 % of maximum current, use neutral density filter if needed). Align LED pulse start with camera triggers, use LED exposure, defined previously. Restore the fixed camera exposure time and enable trigger mode.

   Run a test acquisition to confirm:

a. Even illumination and wavelength-specific disappearance of colored marks
b. No image shift (≤1 pixel)
c. Absence of interference from other devices (test during activation)
d. Stable ROI intensity traces

5. Save your configuration. Archive all camera and system settings for consistent application in future recordings.

4.3. Imaging procedure

1. Prepare the equipment and protocol. Power on all devices and the control computer. Load the imaging protocol and camera settings. Set the save path and enable automatic file naming.
2. Acclimate the animal. Transfer the mouse to the imaging room and allow 30 minutes for habituation.
3. Position and prepare the animal. If required, induce and maintain anesthesia, turn on heating pad and apply ophthalmic gel. Fix the mouse securely in the setup, clean the skull, and protect the eyes with visor (see 1.1.4).

Note: Hand-tightening of holding screws for mouse fixation may be insufficient.

4. Set up the imaging system. Focus the camera, turn on one LED in continuous mode, and switch off ambient lighting.
5. Adjust exposure and LED timing. Optimize exposure for each LED to 70–80 % of the glare threshold (see 4.2.4). Restore the selected exposure and adjust LED pulse durations. Switch to trigger mode.
6. Start recording and minimize disturbance. Begin imaging. Remain quiet and still to avoid external stimulation. Limit total head-fixation time to 1–2 hours.
7. Finish the session and store data. Return the mouse to its home cage and transfer raw data to external storage.

5. Image analysis

Wide-field optical imaging produces sequences of thousands of images. Extracting meaningful signals requires image alignment, noise reduction, and conversion of pixel intensity into relative changes in haemoglobin concentration or sensor fluorescence. Fluorescent signals must also be corrected for haemoglobin absorption (Patent № 2024666595, Russian Federation). Additional challenges include automation, faster analysis, and efficient data storage. While various research groups have developed WFOI analysis pipelines in Matlab and Python, existing open-source scripts lack universality due to variations in hardware, imaging protocols, and analysis methods (Brier & Culver, 2023; Haupt et al., 2017; Xiao et al., 2021). To address this, we developed a Python-based software package tailored for our WFOI setup, described below and available on GitHub (https://github.com/natalia1896/WIFIOPIA). The key stages of the program's operation are listed below.

5.1. Image annotation and brain masking

Due to manual headplate implantation, the accessible cortical area and implantation angle may vary slightly across animals. Additional variability may arise from small shifts in objective positioning between imaging sessions. To enable cross-subject comparisons, images are spatially aligned using anatomical landmarks such as bregma and lambda. These landmarks are manually annotated at the start of analysis, and corresponding rotation and translation parameters are applied to standardize image orientation across sessions. A brain mask is also required to define cortical

regions for analysis. This mask can be generated manually or via automated thresholding or neural network-based segmentation. In our workflow, we use manual annotation via a custom graphical interface, though externally generated binary masks are also supported.

5.2. Image transformation and physiological signal conversion

5.2.1. Image transformation

Based on the annotated landmarks, all images are spatially aligned and sorted into 3D arrays (t, w, h), where each array corresponds to a specific excitation wavelength defined by the illumination protocol. Signal changes are then computed as relative intensity values ($I/I_{t=0}$), where $I_{t=0}$ represents either the mean signal over the full acquisition or over a selected baseline period.

5.2.2. Reflectance signal conversion to haemoglobin concentrations

For dual-wavelength reflectance recordings, relative changes in haemoglobin concentrations (Δ[HbO], Δ[HHb], Δ[HbT]) are calculated using the modified Beer–Lambert law, as described in (Ma et al., 2016):

$$\mu_a = -\frac{1}{X(\lambda)} * \ln\left(\frac{I(\lambda)}{I_0(\lambda)}\right) \quad (1),$$

where μ_a is absorption coefficient, X(λ) - wavelength-dependent pathlength. In our experiments we use wavelength-dependent pathlengths from (Ma et al., 2016). Another step is to solve the following system of equations:

$$\begin{bmatrix} \Delta\mu_a(\lambda_1) \\ \Delta\mu_a(\lambda_2) \end{bmatrix} = \begin{bmatrix} \zeta_{HbO(\lambda_1)} & \zeta_{HHb(\lambda_1)} \\ \zeta_{HbO(\lambda_2)} & \zeta_{HHb(\lambda_2)} \end{bmatrix} * \begin{bmatrix} \Delta[HbO] \\ \Delta[HHb] \end{bmatrix} \quad (2),$$

where $\zeta_{Hb(\lambda)}$ – molar absorption coefficient of specific form of haemoglobin at wavelength λ, $\Delta[HbO], \Delta[HHb]$ – changes (relative to baseline $I_{t=0}$) in molar concentrations of HbO and HHb, respectively, $\Delta\mu_a(\lambda)$ – changes (relative to baseline $I_{t=0}$) in absorption coefficients.

We use tabulated molar extinction coefficient for haemoglobin in water from (*Oregon Medical Laser Center*, n.d.). To calculate $\zeta_{Hb(\lambda)}$ from the tabulated data the following equation was used:

$$\zeta_{Hb(\lambda)} = \ln(10) * \varepsilon_{Hb(\lambda)} \approx 2.303 * \varepsilon_{Hb(\lambda)} \quad (3),$$

where $\zeta_{Hb(\lambda)}$ – molar absorption coefficient (in natural logarithm form), $\varepsilon_{HbO(\lambda)}$ – decadic molar absorption coefficient. Both used in Beer-Lambert law, either in exponential form ($\frac{I(\lambda)}{I_0(\lambda)} = e^{-\zeta * [Hb] * X(\lambda)}$) or Beer-Lambert law in absorbance form ($\frac{I(\lambda)}{I_0(\lambda)} = 10^{-\varepsilon * [Hb] * X(\lambda)}$).

The final solution for the equation is presented below:

$$\Delta[HHb] = \frac{\left(\zeta_{HbO(\lambda_1)} * \Delta\mu_a(\lambda_2) - \zeta_{HbO(\lambda_2)} * \Delta\mu_a(\lambda_1)\right)}{\left(\zeta_{HbO(\lambda_1)} * \zeta_{HHb(\lambda_2)} - \zeta_{HbO(\lambda_2)} * \zeta_{HbR(\lambda_1)}\right)} \quad (4)$$

$$\Delta[HbO] = \frac{\left(\zeta_{HHb(\lambda_1)} * \Delta\mu_a(\lambda_2) - \zeta_{HHb(\lambda_2)} * \Delta\mu_a(\lambda_1)\right)}{\left(\zeta_{HHb(\lambda_1)} * \zeta_{HbO(\lambda_2)} - \zeta_{HHb(\lambda_2)} * \zeta_{HbO(\lambda_1)}\right)} \quad (5)$$

$$\Delta[HbT] = \Delta[HbO] + \Delta[HHb] \quad (6)$$

When only one reflectance wavelength is used, and it lies in the isosbestic range (e.g., 530 nm), changes in $\Delta I/I_{t=0}$ (%) can serve as a proxy for total haemoglobin fluctuations.

5.2.3. Correction of the fluorescence signal for haemoglobin

At present, the search for optimal fluorescence correction methods remains a methodological challenge in the field. Here we describe two such approaches.

Our code includes an implementation of haemoglobin correction based on a modified Beer–Lambert model (Ma et al., 2016):

$$F_{corr} = F_{raw} * e^{(\Delta\mu_a(\lambda_{ex})*X_{ex}+\Delta\mu_a(\lambda_{em})*X_{em})} \ (7),$$

where F_{raw} – raw F/F_0, X_{ex}, X_{em} – photon pathlengths at excitation and emission wavelengths, respectively. However, this approach requires knowledge of the modified excitation and emission photon pathlength (X_{ex}, X_{em}), a parameter that is often experiment-specific and difficult to measure directly (Sunil et al., 2023).

We also implement a data-driven correction using pixel-wise least squares regression (Valley et al., 2020). For each pixel (y, x), a linear model is fit to the observed fluorescence $F_{raw}(t)$ using the corresponding haemodynamic trace Hb(t) (e.g., Δ[HbT] or $\Delta I/I_{t=0}$) as predictor:

$$F_{raw}(t) = \beta_0 + \beta_1 * Hb(t) + \varepsilon(t) \ (8),$$

where β_0, β_1 – coefficients, estimated by linear model, and ε(t) – residuals.

The regression is solved using `np.linalg.lstsq`, minimizing squared residuals. The corrected fluorescence signal is then represented by the residuals after removing the hemodynamic component:

$$F_{corr}(t) = F_{raw}(t) - (\beta_0 + \beta_1 * Hb(t)) \ (9)$$

In our experiments pixel-wise least squares regression demonstrated the best results.

The final output includes percent changes in fluorescence ($\Delta F/F_0$) and haemoglobin concentrations in μM (Δ[HbO], Δ[HHb], Δ[HbT]), or relative reflectance changes ($\Delta I/I_{t=0}$, %) for single-wavelength recordings. Optionally, the global signal (mean intensity across the brain mask) can be subtracted to reduce fluctuations caused by illumination variability. Additional post-processing steps, such as Gaussian smoothing or frequency filtering, can be applied to minimize noise and improve signal quality.

Results

The described protocol for creating a wide cranial window provides an opportunity to accurately measure brain haemodynamics avoiding craniotomy (Fig. 7). During thinning, the diploic vessels are removed, therefore, unrelated to neuron activation haemodynamics does not hide underlying activity. The cancellous bone removing improves image quality, as it contributes substantially to light scattering.

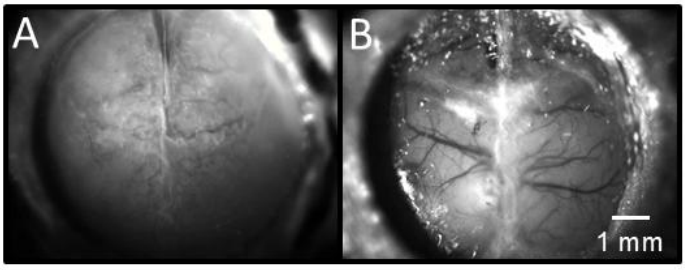

Fig. 7. Representative images of unthinned (A) and thinned (B) scull at 530 nm in light scattering (reflectance) mode. During thinning cancellous bone with diploic vessels is removed.

The scull thinning technique provides optical access for recording cortical activity in the same animal for at least three months (Fig. 8). The durability of the cranial implant ensures stable recordings in awake animals during chronic experiments, withstanding multiple fixation and de-clamping procedures.

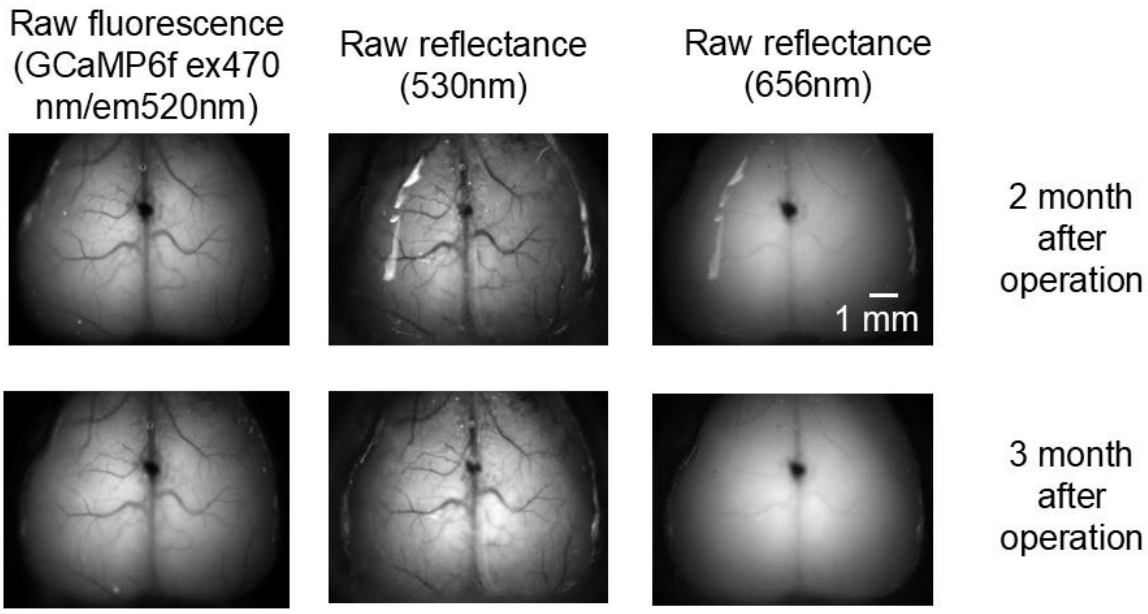

Figure 8. Representative raw images of cranial window. The proposed protocol for creating a wide cranial window enables stable optical access to the mouse cerebral cortex for over three months. Shown are representative raw fluorescence images from the GCaMP6f sensor and light-scatter images acquired under 530 nm and 656 nm illumination, taken two and three months after surgery from the same animal.

The wide cranial window enables the recording of activity across extensive cortical regions in mice, including the motor, somatosensory, parietal, and retrosplenial cortices. To validate the applied brain activity recording and image analysis approaches, we assessed cortical responses to sensory stimulation of different modalities (Fig. 9).

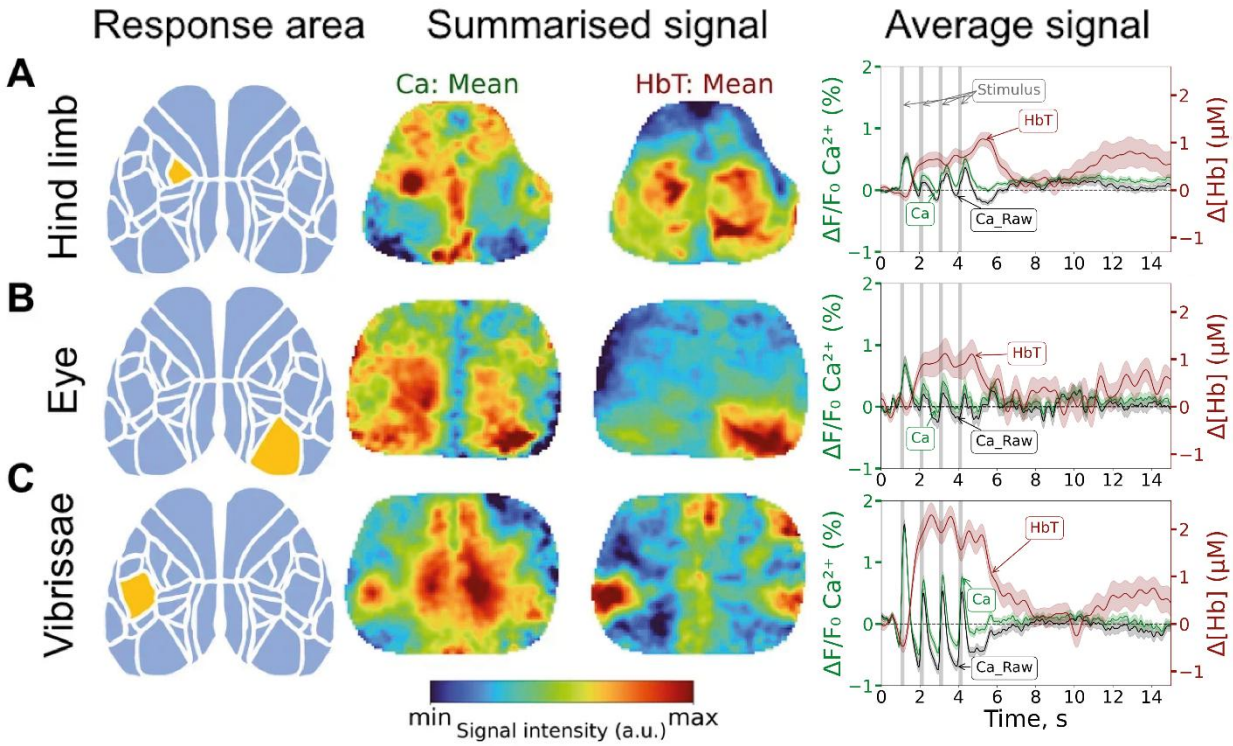

Figure 9. WFOI allows to register responses in the cortex caused by sensory stimuli of different modalities. Responses to stimulation of the right hind limb (**A**), the left eye (**B**) and the right vibrissae (**C**). From left to right are shown: the location of the corresponding response area according to the anatomical atlas (Q. Wang et al., 2020); a summarised calcium and haemodynamic signal during the presentation of the stimulus, normalised from maximum to minimum over 21 repetitions of the stimulus; the average calcium signal from the response area before and after correction to haemodynamics (black and green line, respectively) and haemodynamic response (dark red line).

We successfully recorded localised cortical responses to paw, whisker, and eye stimulation. The spatial distribution of activation areas closely matched the anatomically defined sensory regions for each modality, as referenced in standard brain atlases. Stimulation evoked a calcium signal increase, followed by a localised haemodynamic response indicative of blood influx.

A stimulation protocol was used comprising 21 trains of four short repetitive stimuli (200 ms duration, 1 Hz frequency) was employed. This design enabled precise localisation of response areas.

Importantly, stimulus-evoked responses in awake animals are affected by behavioural state (Fig. 10). The integral measure of calcium response – area under the curve (AUC) – was significantly lower when animals remained behaviourally calm (0.9 ± 1.11 [mean ± SD], $n = 146$), compared to trials involving active locomotion (3.16 ± 2.83, $n = 232$; Welch's t-test: $t(326.4) = -10.90$, $p < 0.0001$; Cohen's $d = -0.97$). A more pronounced effect of movement was observed on the haemodynamic response (measured 0-10 s after stimulation start): AUC of Δ[HbT] was 5.11 ± 15.20 ($n = 146$) during calm responses and 48.91 ± 50.14 ($n = 232$) during locomotion (Welch's t-test: $t(293.4) = -12.43$, $p < 0.0001$; Cohen's $d = -1.08$). Additionally, behavioural activity increased the variability of both calcium and haemodynamic signals, as indicated by Levene's test (calcium: $F = 71.67$, $p < 0.0001$; haemodynamics: $F = 173.63$, $p < 0.0001$).

These findings underscore the importance of monitoring behaviour during recordings. In this study, behavioural state was assessed manually. However, deep learning-based tools such as DeepLabCut (Mathis et al., 2018) could offer a more objective and reproducible approach for future behavioural classification.

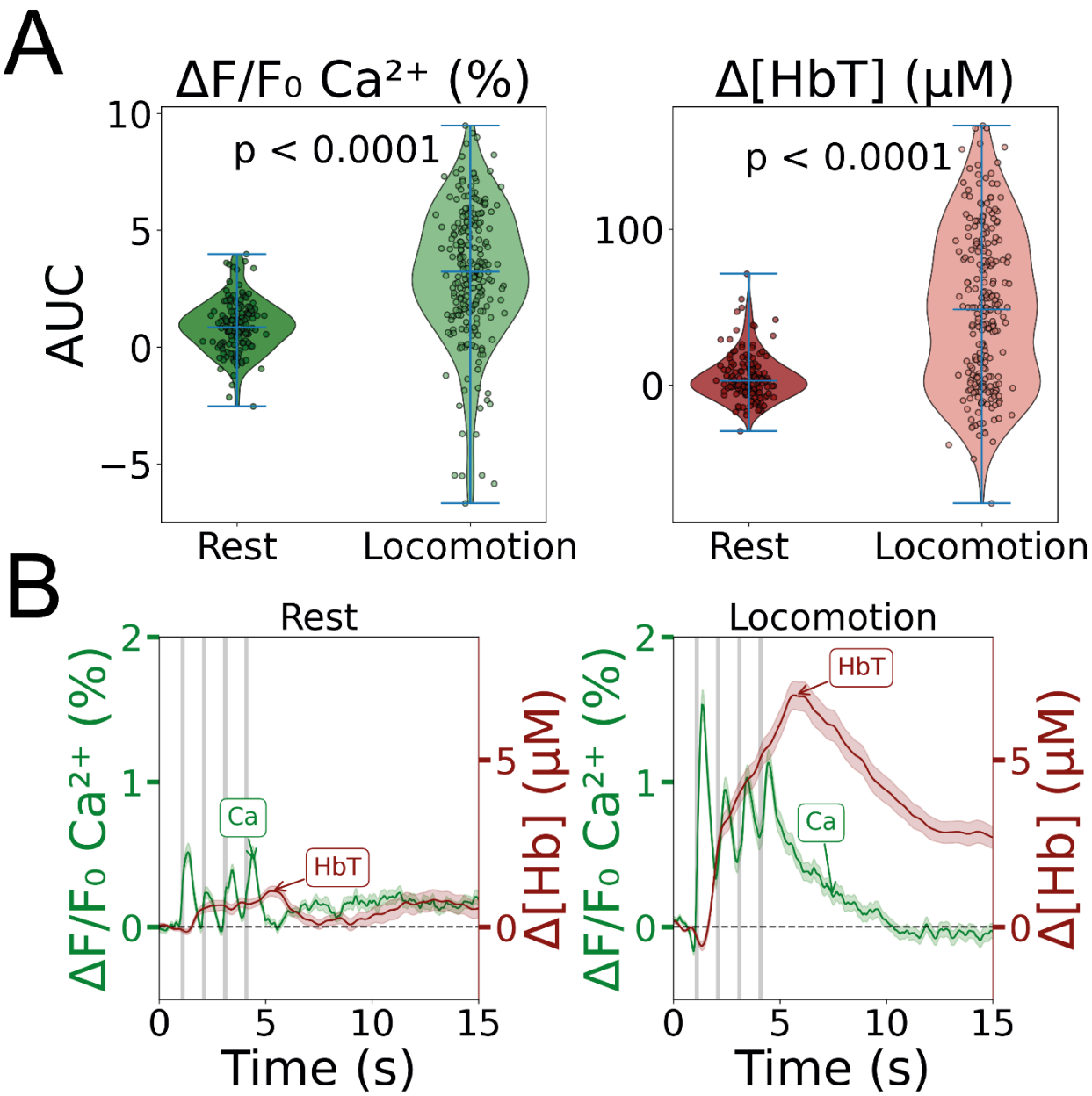

Figure 10. Behaviour significantly affects WFOI responses to stimulation. (**A**) Violin plots showing the area under the curve (AUC) of individual calcium and haemodynamic responses of somatosensory cortex for hind limb stimulation during calm behaviour (Rest) and active locomotion (Locomotion). (**B**) Responses to stimulation of the hind limbs: averaged Ca^{2+} signal from the response area (green line) and the corresponding haemodynamic response (dark red line), shown for both Rest and Locomotion conditions. Data were collected from 8 mice with stimulation applied to both left and right limbs (21 repetitions of 4 pulses with 200 ms duration, 1 Hz frequency, I = 90 μA for each limb); responses were recorded from the somatosensory cortex contralateral to the side of stimulation. P-values are based on Welch's t-test.

Discussion

There are two principal approaches to creating cranial windows: transcranial windows, which preserve the skull (Grinvald et al., 1986), and craniotomies involving skull removal (J. H. Kim et al., 1989). Two-photon microscopy typically requires skull thinning (Kelly & Majewska, 2010) or removal with a glass-covered craniotomy (Holtmaat et al., 2009; Mikkelsen et al., 2022). Wide-field optical imaging (WFOI), by contrast, benefits from large cranial windows that expose up to 40–80% of the cortical surface.

While protocols for intrinsic imaging through the intact skull exist (Silasi et al., 2016; White et al., 2011), our observations suggest that variability in diploic vessels may obscure neural signals. Additionally, intact skull bone significantly reduces signal strength and signal-to-noise ratio. Removing the trabecular (spongy) bone layer improves optical clarity and can be achieved via skull thinning (Shahsavarani et al., 2023) or skull replacement with transparent materials such as silicone (Manita et al., 2022), nanocoatings (Takahashi et al., 2021), PDMS (polydimethylsiloxane), (Heo et al., 2016; Yang et al., 2022), PET plastic (Ghanbari et al., 2019), polymethylpentene (Edelman et al., 2024), or glass (T. H. Kim et al., 2016). Chemical skull clearing methods have also been developed (Cramer et al., 2021; C. Zhang et al., 2018).

Although skull thinning techniques have been described (Kozberg et al., 2016; Shahsavarani et al., 2023), detailed protocols are often lacking. The method we present is technically simpler than full cranial replacement, carries a lower risk of infection, and minimises bleeding – when performed with proper skill. A key feature of our protocol is the use of non-fluorescent gel-based nail polish as a transparent and protective coating. While this approach is optimised for WFOI (particularly laser contrast imaging), it may also be compatible with two-photon microscopy. Potential limitations include the risk of neuroinflammation, dura mater opacification due to pressure, and long-term bone regrowth. The procedure is time-consuming at first but becomes efficient with practice. We demonstrated the method is suitable for both recording evoked responses to sensory stimulation and for chronic longitudinal imaging. The window remains optically stable and functional for extended periods, enabling repeated within-subject measurements.

Independent of the cranial window technique, stable head fixation is essential for high-quality imaging. This is typically achieved by attaching a fixation device during surgery, which is later mounted in a stereotaxic holder or mounting frame under the microscope. Devices vary in form—screws, nuts (Silasi et al., 2016), plates (Kelly & Majewska, 2010; Manita et al., 2022; Takahashi et al., 2021), or custom clip-based holders (Ghanbari et al., 2019; Mikkelsen et al., 2022). We modified commercial headplates (Neurotar, Finland), originally designed like helicopter blades, to increase cortical access while ensuring firm fixation. These lightweight, compact plates are compatible with the Mobile HomeCage® (Neurotar, Finland).

WFOI system design varies depending on experimental goals. While commercial systems are available (e.g. Invigilo 3, Neurotar, Finland; OASIS Macro Cortex-Wide Intrinsic Optical Imaging, Mightex, CA, USA), many laboratories build custom setups that support intrinsic imaging, calcium or FAD imaging, stroke induction, and other procedures (Shahsavarani et al., 2023; X. Wang et al., 2024; Zhao et al., 2021), including low-cost configurations (Harrison et al., 2009). Various solutions for awake mice *in vivo* imaging exist: rotating disks (Heo et al., 2016; Nietz et al., 2022), spheres (Dombeck et al., 2007), cylinders (Cardin et al., 2020), treadmills (Fedotova et al., 2023; Moeini et al., 2020; Yi et al., 2024), hovercraft platforms (Juczewski et al., 2020; Stuart et al., 2024), and even hammocks (Padawer-Curry et al., 2023) or tubes (Silasi et al., 2016). WFOI is also compatible with virtual reality setups (Pinke et al., 2023).

We developed a flexible and cost-effective WFOI system using commercially available components, which can be readily adapted to various experimental needs. While high-end systems can exceed $200,000, our protocol outlines a minimal configuration suitable for constrained budgets.

We hope that this accessible and adaptable approach will promote broader use of functional imaging techniques in neuroscience research, contributing to a deeper understanding of brain function and disease mechanisms.

Supplementary data

Supplementary data is available at Biology Methods and Protocols online.

Data availability

Supplementary video materials are available at YouTube channel “WIFIOPIA”: https://www.youtube.com/@WIFIOPIA.

Code described in this article and sample data have been deposited to GitHub https://github.com/natalia1896/WIFIOPIA). Any additional data, if needed, will be provided upon request.

Conflict of Interest

The authors declare that the research was conducted in the absence of any commercial or financial relationships that could be construed as a potential conflict of interest.

Author Contributions

Kislukhina E.N. (Methodology [equal], Validation [equal], Data curation [equal], Investigation [equal], 3D-Modeling [lead], Visualisation [lead], Writing-original draft [equal]); **Lizunova N.V.** (Methodology [equal], Validation [equal], Data curation [equal], Investigation [equal], Writing-original draft [supporting], Programming [lead]); **Surin A.M.** (Conceptualization [lead], Supervision [equal], Writing - review & editing [equal]); **Bakaeva Z.V.** (Conceptualization [equal], Data curation [equal], Supervision [lead], Writing - review & editing [equal], Project administration [lead]).

Funding

This research was funded by the Ministry of Health of the Russian Federation, the project № AAAA-A19-119012590191-3, by the Ministry of Science and Higher Education of the Russian Federation № 08-07-S6/2021/82930, "the grant in the form of subsidies for the implementation of activities aimed at updating the equipment base of leading organizations conducting scientific research" and by the grant № FGFU-2025-0004.

Institutional Review Board Statement

The study was conducted in accordance with the ethical principles and regulatory documents recommended by the European Science Foundation (ESF) and the Declaration on Humane Treatment of Animals and in accordance with the Order of the Ministry of Health and Social Development of Russia № 708n of August 23, 2010 “On Approval of Laboratory Practices”. Animal care, breeding and experimental procedures were carried out as required of the Ethical committee of the Institute of General Pathology and Pathophysiology, Protocol № 05-06/12 of 14.12.2017 and the Ethical committee of the National Medical Research Center for Children’s Health, Protocol № 05 of 15.05.2025

Acknowledgments

The authors gratefully acknowledge prof. Piotr Brezhestovskiĭ for generously enabling access to the ClopHensor mouse line, and for his valuable methodological insights and suggestions. The authors thank Dr. Leonard Khiroug, whose ideas and efforts provided the initial impetus for this

research. Some portions of this manuscript, including language polishing, and draft code documentation (e.g., function docstrings), were assisted using ChatGPT (OpenAI, San Francisco, CA). Final decisions and edits were made by the authors.

References

Arosio, D., Ricci, F., Marchetti, L., Gualdani, R., Albertazzi, L., & Beltram, F. (2010). Simultaneous intracellular chloride and pH measurements using a GFP-based sensor. *Nature Methods*, *7*(7), 516–518. https://doi.org/10.1038/nmeth.1471

Brier, L. M., & Culver, J. P. (2023). Open-source statistical and data processing tools for wide-field optical imaging data in mice. *Neurophotonics*, *10*(01), 016601–016601. https://doi.org/10.1117/1.nph.10.1.016601

Cardin, J. A., Crair, M. C., & Higley, M. J. (2020). Mesoscopic Imaging: Shining a Wide Light on Large-Scale Neural Dynamics. In *Neuron* (Vol. 108, Issue 1). https://doi.org/10.1016/j.neuron.2020.09.031

Chance, B., Schoener, B., Oshino, R., Itshak, F., & Nakase, Y. (1979). Oxidation-reduction ratio studies of mitochondria in freeze-trapped samples. NADH and flavoprotein fluorescence signals. *The Journal of Biological Chemistry*, *254*(11). https://doi.org/10.1016/s0021-9258(17)30079-0

Chroma Technology. (n.d.). Retrieved July 10, 2025, from https://www.chroma.com/products/filter-set-types/bandpass-sets/longpass-filter-sets

Cramer, S. W., Carter, R. E., Aronson, J. D., Kodandaramaiah, S. B., Ebner, T. J., & Chen, C. C. (2021). Through the looking glass: A review of cranial window technology for optical access to the brain. In *Journal of Neuroscience Methods* (Vol. 354). https://doi.org/10.1016/j.jneumeth.2021.109100

D. Edelstein, A., A. Tsuchida, M., Amodaj, N., Pinkard, H., D. Vale, R., & Stuurman, N. (2014). Advanced methods of microscope control using μManager software. *Journal of Biological Methods*, *1*(2). https://doi.org/10.14440/jbm.2014.36

Dana, H., Chen, T.-W., Hu, A., Shields, B. C., Guo, C., Looger, L. L., Kim, D. S., & Svoboda, K. (2014). Thy1-GCaMP6 Transgenic Mice for Neuronal Population Imaging In Vivo. *PLoS ONE*, *9*(9), e108697. https://doi.org/10.1371/journal.pone.0108697

Day-Cooney, J., Dalangin, R., Zhong, H., & Mao, T. (2023). Genetically encoded fluorescent sensors for imaging neuronal dynamics in vivo. In *Journal of Neurochemistry* (Vol. 164, Issue 3). https://doi.org/10.1111/jnc.15608

Diuba, A. V., Samigullin, D. V., Kaszas, A., Zonfrillo, F., Malkov, A., Petukhova, E., Casini, A., Arosio, D., Esclapez, M., Gross, C. T., & Bregestovski, P. (2020a). CLARITY analysis of the Cl/pH sensor expression in the brain of transgenic mice. *Neuroscience*, *439*. https://doi.org/10.1016/j.neuroscience.2019.07.010

Diuba, A. V, Samigullin, D. V, Kaszas, A., Zonfrillo, F., Malkov, A., Petukhova, E., Casini, A., Arosio, D., Esclapez, M., Gross, C. T., & Bregestovski, P. (2020b). CLARITY analysis of the Cl/pH sensor expression in the brain of transgenic mice. *Neuroscience*, *439*. https://doi.org/10.1016/j.neuroscience.2019.07.010

Dombeck, D. A., Khabbaz, A. N., Collman, F., Adelman, T. L., & Tank, D. W. (2007). Imaging Large-Scale Neural Activity with Cellular Resolution in Awake, Mobile Mice. *Neuron*, *56*(1). https://doi.org/10.1016/j.neuron.2007.08.003

Edelman, B. J., Siegenthaler, D., Wanken, P., Jenkins, B., Schmid, B., Ressle, A., Gogolla, N., Frank, T., & Macé, E. (2024). The COMBO window: A chronic cranial implant for multiscale circuit interrogation in mice. *PLoS Biology*, *22*(6), e3002664.

Fedotova, A., Brazhe, A., Doronin, M., Toptunov, D., Pryazhnikov, E., Khiroug, L., Verkhratsky, A., & Semyanov, A. (2023). Dissociation Between Neuronal and Astrocytic Calcium Activity in Response to Locomotion in Mice. *Function*, *4*(4), zqad019. https://doi.org/10.1093/function/zqad019

FPbase. (n.d.). Retrieved July 10, 2025, from https://www.fpbase.org/

Ghanbari, L., Carter, R. E., Rynes, M. L., Dominguez, J., Chen, G., Naik, A., Hu, J., Sagar, M. A. K., Haltom, L., Mossazghi, N., Gray, M. M., West, S. L., Eliceiri, K. W., Ebner, T. J., & Kodandaramaiah, S. B. (2019). Cortex-wide neural interfacing via transparent polymer skulls. *Nature Communications*, *10*(1). https://doi.org/10.1038/s41467-019-09488-0

Grinvald, A., Lieke, E., Frostig, R. D., Gilbert, C. D., & Wiesel, T. N. (1986). Functional architecture of cortex revealed by optical imaging of intrinsic signals. *Nature*, *324*(6095), 361–364. https://doi.org/10.1038/324361a0

Harrison, T. C., Sigler, A., & Murphy, T. H. (2009). Simple and cost-effective hardware and software for functional brain mapping using intrinsic optical signal imaging. *Journal of Neuroscience Methods*, *182*(2), 211–218. https://doi.org/10.1016/J.JNEUMETH.2009.06.021

Haupt, D., Vanni, M. P., Bolanos, F., Mitelut, C., LeDue, J. M., & Murphy, T. H. (2017). Mesoscale brain explorer, a flexible python-based image analysis and visualization tool. *Neurophotonics*, *4*(3), 031210. https://doi.org/10.1117/1.NPh.4.3.031210

Heo, C., Park, H., Kim, Y. T., Baeg, E., Kim, Y. H., Kim, S. G., & Suh, M. (2016). A soft, transparent, freely accessible cranial window for chronic imaging and electrophysiology. *Scientific Reports*, *6*. https://doi.org/10.1038/srep27818

Holtmaat, A., Bonhoeffer, T., Chow, D. K., Chuckowree, J., De Paola, V., Hofer, S. B., Hübener, M., Keck, T., Knott, G., Lee, W. C. A., Mostany, R., Mrsic-Flogel, T. D., Nedivi, E., Portera-Cailliau, C., Svoboda, K., Trachtenberg, J. T., & Wilbrecht, L. (2009). Long-term, high-resolution imaging in the mouse neocortex through a chronic cranial window. *Nature Protocols*, *4*(8). https://doi.org/10.1038/nprot.2009.89

Juczewski, K., Koussa, J. A., Kesner, A. J., Lee, J. O., & Lovinger, D. M. (2020). Stress and behavioral correlates in the head-fixed method: stress measurements, habituation dynamics, locomotion, and motor-skill learning in mice. *Scientific Reports*, *10*(1). https://doi.org/10.1038/s41598-020-69132-6

Kelly, E. A., & Majewska, A. K. (2010). Chronic imaging of mouse visual cortex using a thinned-skull preparation. *Journal of Visualized Experiments*, *44*. https://doi.org/10.3791/2060

Khiroug, L., & Verkhratsky, A. (2021). Coming full circle: In vivo Veritas, or expanding the neuroscience frontier. *Cell Calcium*, *98*. https://doi.org/10.1016/j.ceca.2021.102452

Kim, J. H., Dunn, M. B., Hua, Y., Rydberg, J., Yae, H., Elias, S. A., & Ebner, T. J. (1989). Imaging of cerebellar surface activation In vivo using voltage sensitive dyes. *Neuroscience*, *31*(3). https://doi.org/10.1016/0306-4522(89)90427-2

Kim, T. H., Zhang, Y., Lecoq, J., Jung, J. C., Li, J., Zeng, H., Niell, C. M., & Schnitzer, M. J. (2016). Long-Term Optical Access to an Estimated One Million Neurons in the Live Mouse Cortex. *Cell Reports*, *17*(12), 3385–3394. https://doi.org/10.1016/j.celrep.2016.12.004

Kislukhina, E. N., Lizunova, N. V., Lisina, O. Yu., Sharipov, R. R., Krasilnikova, I. A., Bakaeva, Z. V., Pinelis, V. G., & Surin, A. M. (2023). Glutamate and ischemia-induced changes in ion homeostasis in the neuronal culture and cerebral cortex of mice expressing Ca2+-sensor GCaMP6f. *Patologicheskaya Fiziologiya i Eksperimental'naya Terapiya (Pathological physiology and experimental therapy)*, *67*(1), 5–20. https://doi.org/10.25557/0031-2991.2023.01.5-20

Kotova, D. A., Ivanova, A. D., Pochechuev, M. S., Kelmanson, I. V., Khramova, Y. V., Tiaglik, A., Sudoplatov, M. A., Trifonova, A. P., Fedotova, A., Morozova, K., Katrukha, V. A., Sergeeva, A. D., Raevskii, R. I., Pestriakova, M. P., Solotenkov, M. A., Stepanov, E. A., Tsopina, A. S., Moshchenko, A. A., Shestopalova, M., … Bilan, D. S. (2023). Hyperglycemia exacerbates ischemic stroke not through increased generation of hydrogen peroxide. *Free Radical Biology and Medicine*, *208*. https://doi.org/10.1016/j.freeradbiomed.2023.08.004

Kozberg, M. G., Ma, Y., Shaik, M. A., Kim, S. H., & Hillman, E. M. C. (2016). Rapid Postnatal Expansion of Neural Networks Occurs in an Environment of Altered Neurovascular and Neurometabolic Coupling. *The Journal of Neuroscience : The Official Journal of the Society for Neuroscience*, *36*(25), 6704–6717. https://doi.org/10.1523/JNEUROSCI.2363-15.2016

Li, R., Yang, D., Fang, F., Hong, K. S., Reiss, A. L., & Zhang, Y. (2022). Concurrent fNIRS and EEG for Brain Function Investigation: A Systematic, Methodology-Focused Review. In *Sensors* (Vol. 22, Issue 15). https://doi.org/10.3390/s22155865

Ma, Y., Shaik, M. A., Kim, S. H., Kozberg, M. G., Thibodeaux, D. N., Zhao, H. T., Yu, H., & Hillman, E. M. C. (2016). Wide-field optical mapping of neural activity and brain haemodynamics: considerations and novel approaches. *Philosophical Transactions of the Royal Society B: Biological Sciences*, *371*(1705), 20150360. https://doi.org/10.1098/rstb.2015.0360

Manita, S., Shigetomi, E., Bito, H., Koizumi, S., & Kitamura, K. (2022). In Vivo Wide-Field and Two-Photon Calcium Imaging from a Mouse using a Large Cranial Window. *Journal of Visualized Experiments*, *2022*(186). https://doi.org/10.3791/64224

Markicevic, M., Savvateev, I., Grimm, C., & Zerbi, V. (2021). Emerging imaging methods to study whole-brain function in rodent models. In *Translational Psychiatry* (Vol. 11, Issue 1). https://doi.org/10.1038/s41398-021-01575-5

Marvin, J. S., Scholl, B., Wilson, D. E., Podgorski, K., Kazemipour, A., Müller, J. A., Schoch, S., Quiroz, F. J. U., Rebola, N., Bao, H., Little, J. P., Tkachuk, A. N., Cai, E., Hantman, A. W., Wang, S. S. H., DePiero, V. J., Borghuis, B. G., Chapman, E. R., Dietrich, D., … Looger, L. L. (2018). Stability, affinity, and chromatic variants of the glutamate sensor iGluSnFR. *Nature Methods*, *15*(11). https://doi.org/10.1038/s41592-018-0171-3

Mathis, A., Mamidanna, P., Cury, K. M., Abe, T., Murthy, V. N., Mathis, M. W., & Bethge, M. (2018). DeepLabCut: markerless pose estimation of user-defined body parts with deep learning. *Nature Neuroscience 2018 21:9*, *21*(9), 1281–1289. https://doi.org/10.1038/s41593-018-0209-y

Mikkelsen, S. H., Wied, B., Dashkovskyi, V., Lindhardt, T. B., Hirschler, L., Warnking, J. M., Barbier, E. L., Postnov, D., Hansen, B., & Gutiérrez-Jiménez, E. (2022). Head holder and cranial window design for sequential magnetic resonance imaging and optical imaging in awake mice. *Frontiers in Neuroscience*, *16*. https://doi.org/10.3389/fnins.2022.926828

Moeini, M., Cloutier-Tremblay, C., Lu, X., Kakkar, A., & Lesage, F. (2020). Cerebral tissue pO2 response to treadmill exercise in awake mice. *Scientific Reports*, *10*(1). https://doi.org/10.1038/s41598-020-70413-3

Nietz, A. K., Popa, L. S., Streng, M. L., Carter, R. E., Kodandaramaiah, S. B., & Ebner, T. J. (2022). Wide-Field Calcium Imaging of Neuronal Network Dynamics In Vivo. *Biology*, *11*(11), 1601. https://doi.org/10.3390/biology11111601

Oregon Medical Laser Center. (n.d.). Retrieved July 10, 2025, from https://omlc.org/spectra/hemoglobin/summary.html

Padawer-Curry, J. A., Bowen, R. M., Jarang, A., Wang, X., Lee, J. M., & Bauer, A. Q. (2023). Wide-Field Optical Imaging in Mouse Models of Ischemic Stroke. *Methods in Molecular Biology (Clifton, N.J.)*, *2616*, 113–151. https://doi.org/10.1007/978-1-0716-2926-0_11

Pinke, D., Issa, J. B., Dara, G. A., Dobos, G., & Dombeck, D. A. (2023). Full field-of-view virtual reality goggles for mice. *Neuron*, *111*(24). https://doi.org/10.1016/j.neuron.2023.11.019

Ponomareva, D., Petukhova, E., & Bregestovski, P. (2021). Simultaneous monitoring of ph and chloride (Cl^-) in brain slices of transgenic mice. *International Journal of Molecular Sciences*, *22*(24). https://doi.org/10.3390/ijms222413601

Shahsavarani, S., Thibodeaux, D. N., Xu, W., Kim, S. H., Lodgher, F., Nwokeabia, C., Cambareri, M., Yagielski, A. J., Zhao, H. T., Handwerker, D. A., Gonzalez-Castillo, J., Bandettini, P. A., & Hillman, E. M. C. (2023). Cortex-wide neural dynamics predict behavioral states and provide a neural basis for resting-state dynamic functional connectivity. *Cell Reports*, *42*(6). https://doi.org/10.1016/j.celrep.2023.112527

Silasi, G., Xiao, D., Vanni, M. P., Chen, A. C. N., & Murphy, T. H. (2016). Intact skull chronic windows for mesoscopic wide-field imaging in awake mice. *Journal of Neuroscience Methods*, *267*, 141–149. https://doi.org/10.1016/j.jneumeth.2016.04.012

Stuart, S. A., Palacios-Filardo, J., Domanski, A., Udakis, M., Duguid, I., Jones, M. W., & Mellor, J. R. (2024). Hippocampal-dependent navigation in head-fixed mice using a floating real-world environment. *Scientific Reports*, *14*(1), 14315.

Sunil, S., Jiang, J., Shah, S., Kura, S., Kilic, K., Erdener, S. E., Ayata, C., Devor, A., & Boas, D. A. (2023). Neurovascular coupling is preserved in chronic stroke recovery after targeted photothrombosis. *NeuroImage: Clinical*, *38*, 103377. https://doi.org/10.1016/j.nicl.2023.103377

Takahashi, T., Zhang, H., Otomo, K., Okamura, Y., & Nemoto, T. (2021). Protocol for constructing an extensive cranial window utilizing a PEO-CYTOP nanosheet for in vivo wide-field imaging of the mouse brain. *STAR Protocols*, *2*(2). https://doi.org/10.1016/j.xpro.2021.100542

Valley, M. T., Moore, M. G., Zhuang, J., Mesa, N., Castelli, D., Sullivan, D., Reimers, M., & Waters, J. (2020). Separation of hemodynamic signals from GCaMP fluorescence measured with wide-field imaging. *Journal of Neurophysiology*, *123*(1), 356–366. https://doi.org/10.1152/JN.00304.2019

Wang, Q., Ding, S. L., Li, Y., Royall, J., Feng, D., Lesnar, P., Graddis, N., Naeemi, M., Facer, B., Ho, A., Dolbeare, T., Blanchard, B., Dee, N., Wakeman, W., Hirokawa, K. E., Szafer, A., Sunkin, S. M., Oh, S. W., Bernard, A., … Ng, L. (2020). The Allen Mouse Brain Common Coordinate Framework: A 3D Reference Atlas. *Cell*, *181*(4), 936–953. https://doi.org/10.1016/j.cell.2020.04.007

Wang, X., Padawer-Curry, J. A., Bice, A. R., Kim, B., Rosenthal, Z. P., Lee, J.-M., Goyal, M. S., Macauley, S. L., & Bauer, A. Q. (2024). Spatiotemporal relationships between neuronal, metabolic, and hemodynamic signals in the awake and anesthetized mouse brain. *Cell Reports*, *43*(9).

White, B. R., Bauer, A. Q., Snyder, A. Z., Schlaggar, B. L., Lee, J.-M., & Culver, J. P. (2011). Imaging of Functional Connectivity in the Mouse Brain. *PLoS ONE*, *6*(1), e16322. https://doi.org/10.1371/journal.pone.0016322

Xiao, D., Forys, B. J., Vanni, M. P., & Murphy, T. H. (2021). MesoNet allows automated scaling and segmentation of mouse mesoscale cortical maps using machine learning. *Nature Communications 2021 12:1*, *12*(1), 1–13. https://doi.org/10.1038/s41467-021-26255-2

Yang, N., Liu, F., Zhang, X., Chen, C., Xia, Z., Fu, S., Wang, J., Xu, J., Cui, S., Zhang, Y., Yi, M., Wan, Y., Li, Q., & Xu, S. (2022). A Hybrid Titanium-Softmaterial, High-Strength, Transparent Cranial Window for Transcranial Injection and Neuroimaging. *Biosensors*, *12*(2), 129. https://doi.org/10.3390/bios12020129

Yi, Y., Zhang, Y., Song, Y., & Lu, Y. (2024). Treadmill Running Regulates Adult Neurogenesis, Spatial and Non-spatial Learning, Parvalbumin Neuron Activity by ErbB4 Signaling. *Cellular and Molecular Neurobiology*, *44*(1). https://doi.org/10.1007/s10571-023-01439-0

Zhang, C., Feng, W., Zhao, Y., Yu, T., Li, P., Xu, T., Luo, Q., & Zhu, D. (2018). A large, switchable optical clearing skull window for cerebrovascular imaging. *Theranostics*, *8*(10). https://doi.org/10.7150/thno.23686

Zhang, Y., Rózsa, M., Liang, Y., Bushey, D., Wei, Z., Zheng, J., Reep, D., Broussard, G. J., Tsang, A., Tsegaye, G., Narayan, S., Obara, C. J., Lim, J. X., Patel, R., Zhang, R., Ahrens, M. B., Turner, G. C., Wang, S. S. H., Korff, W. L., … Looger, L. L. (2023). Fast and sensitive GCaMP calcium indicators for imaging neural populations. *Nature*, *615*(7954), 884–891. https://doi.org/10.1038/s41586-023-05828-9

Zhao, H. T., Tuohy, M. C., Chow, D., Kozberg, M. G., Kim, S. H., Shaik, M. A., & Hillman, E. M. C. (2021). Neurovascular dynamics of repeated cortical spreading depolarizations after acute brain injury. *Cell Reports*, *37*(1), 109794. https://doi.org/10.1016/j.celrep.2021.109794